Temporal changes of seismic velocity and anisotropy in the shallow crust induced by the 1999 October 22 *M*6.4 Chia-Yi, Taiwan earthquake

Kevin Chao and Zhigang Peng

School of Earth and Atmospheric Sciences, Georgia Institute of Technology, Atlanta, GA 30332, USA. E-mail: kevinchao@gatech.edu

SUMMARY

Observing temporal changes of material properties in the upper crust has been a long-sought goal within the geophysics community for many decades. A better quantification of temporal changes in the near-surface layers associated with nearby large earthquakes is crucial for improved understandings of rock rheology in the shallow crust, better characterization of site response, and accurate predictions of strong ground motions for future large earthquakes. We systematically analyse temporal changes of seismic velocity and anisotropy in the shallow crust in southwest Taiwan using local earthquakes recorded at a 200-m-deep borehole station CHY. This station is located directly above the hypocentre of the 1999 October 22, *M*6.4 Chia-Yi earthquake. Three-component seismograms recorded at this station show clear direct (upgoing) and surface-reflected (downgoing) *P* and *S* waves, and *S*-wave splitting signals. We use the time delays between the upgoing and downgoing waves in the autocorrelation functions as the proxies for the two-way traveltimes in the top 200 m. The *S*-wave traveltimes measured in two horizontal components increase by ∼1–2 per cent at the time of Chia-Yi main shock, and followed by a logarithmic recovery, while the temporal changes of *S*-wave splitting and *P*-wave traveltimes are less than 1 per cent and are not statistically significant. We obtain similar results by grouping earthquakes into clusters according to their locations and waveform similarities. This suggests that the observed temporal changes are not very sensitive to the seismic ray paths below CHY, but are mostly controlled by the variation of material properties in the top 200 m of the crust. We propose that strong ground motions of the Chia-Yi main shock cause transient openings of fluid-filled microcracks and increases the porosity in the near-surface layers, followed by logarithemic recovery processes. No clear change in the delay times of the shear wave anisotropy is found following the main shock, suggesting that cracks opened during the earthquake do not have a preferred orientation. Our results also show a gradual increase of time delays for both the fast and slow *S* waves in the 7 yr prior to the Chia-Yi main shock. Such changes might be caused by variations of water table, sediment packing or other surficial processes.

Key words: Earthquake ground motions; Seismic anisotropy; Site effects; Wave propagation; Fractures and faults.

1 INTRODUCTION

The top few hundred metres of the shallow crust is heavily fractured, and is characterized by extremely low shear wave velocity ($\sim$200–400 m s^{-1}) and very high attenuation ($Q \sim$ 1–10) (e.g. Aster & Shearer 1991b). If the fractures are preferentially aligned, seismic shear waves propagating through such shallow anisotropic layer are expected to split into two orthogonally polarized waves travelling at different velocities. This phenomenon is analogous to optical birefringence and is termed shear wave splitting (SWS). Two routinely determined splitting parameters are the polarization

direction of the fast wave (ϕ) and the delay time (δt) between the fast and slow waves. SWS in the shallow crust can be caused by different mechanisms, such as extrinsic (e.g. structural controlled or stress induced) anisotropy (e.g. Crampin 1987; Zinke & Zoback 2000; Boness & Zoback 2006) or intrinsic (e.g. aligned crystal or grain) anisotropy (Kern & Wenk 1990; Savage 1999; Valcke *et al.* 2006; Hall *et al.* 2008). The obtained magnitude of shear wave anisotropy in the shallow crust is typically in the range of 5–20 per cent, and decreases systematically with increasing depth (e.g. Daley & McEvilly 1990; Aster & Shearer 1991a; Coutant 1996; Boness & Zoback 2004, 2006; Liu *et al.* 2004, 2005a;

GJI Seismology

Peng & Ben-Zion 2004). This is mainly because increasing normal stress at depth tends to close fractures and microcracks, resulting in reduced shear wave anisotropy. The elastic and anisotropic properties of the shallow crust can be further modulated by strong ground motions of nearby earthquakes, and other processes that operate under very low normal stress conditions. These include changes in the water table, weathering processes, seasonal thermoelastic strain and solid earth tides.

Observing temporal changes of material properties in the upper crust has been a long-sought goal within the geophysics community for many decades. A better quantification of temporal changes in the near-surface layers is crucial for improved understandings of rock rheology in the shallow crust, better characterization of site responses and accurate predictions of strong ground motions for future large earthquakes. Numerous laboratory studies over the past few decades have found a clear stress dependence of elastic and anisotropic properties for crustal rocks and near-surface layers (e.g. Scholz 1968; Nur & Simmons 1969). Such stress dependence is mainly caused by the opening/closure of microcracks or changes of porosity due to changes in normal stresses (e.g. Nur 1971; Crampin & Zatsepin 1997). Because of this, it is possible to detect temporal changes of material properties and stress variations by monitoring time-varying seismic properties.

Using natural earthquake sources, many earlier studies have observed large temporal changes in the traveltimes of *P* and *S* arrivals, or scattering properties in the *S*-coda waves (e.g. Whitcomb *et al.* 1973; Jin & Aki 1986). However, these studies were not generally convincing, mainly due to uncertainties associated with earthquake locations and origin times (e.g. McEvilly & Johnson 1974; Kanamori & Fuis 1976; Beroza *et al.* 1995). Recent studies based on waveform cross-correlations of repeating earthquakes have found small but resolvable changes of seismic velocities in shallow surface layers and around active fault zones associated with the occurrences of major earthquakes or aseismic slip events (e.g. Poupinet *et al.* 1984; Niu *et al.* 2003; Rubinstein & Beroza 2004a,b, 2005; Schaff & Beroza 2004; Li *et al.* 2006; Peng & Ben-Zion 2006; Rubinstein *et al.* 2007; Taira *et al.* 2008, 2009; Toteva *et al.* 2008; Zhao & Peng 2009). The observed temporal changes in seismic velocities, typically on the order of a few per cent or less, are characterized by rapid reductions during strong motions of nearby large earthquakes, followed by logarithmic recoveries on the timescales of several months to years. The use of repeating earthquakes allows the separation of temporal changes of material properties from spatial variations of earthquake locations (e.g. Liu *et al.* 2004, 2005a; Peng & Ben-Zion 2005, 2006). However, repeating earthquakes only occur in certain locations and their occurrence times cannot be controlled. Some recent studies also employed repeating artificial sources (e.g. Li *et al.* 1998, 2006; Matsumoto *et al.* 2001; Vidale & Li 2003; Silver *et al.* 2007; Niu *et al.* 2008) and found similar results. However these types of studies are limited by high cost and poor depth penetration.

While temporal changes of seismic velocities in the shallow crust have been well documented, the results on temporal changes of SWS are still controversial. Using natural earthquakes, a number of studies have found temporal changes of splitting parameters before (e.g. Crampin *et al.* 1990, 1991, 1999; Gao *et al.* 1998; Crampin & Gao 2005), during (e.g. Saiga *et al.* 2003) and after (e.g. Tadokoro & Ando 2002; Hiramatsu *et al.* 2005) major events or earthquake swarms. In addition, Teanby *et al.* (2004) observed clear temporal changes in SWS parameters in a borehole, and suggested that tidal forces and oil production processes could cause such temporal changes. Recent studies have also shown clear temporal changes in anisotropy parameters associated with volcanic eruptions or earth-

quake swarms in volcanic regions (Miller & Savage 2001; Del Pezzo *et al.* 2004; Gerst & Savage 2004). However, other studies did not find any clear changes of crustal anisotropy near the epicentral regions of major earthquakes (e.g. Aster *et al.* 1990, 1991; Savage *et al.* 1990; Munson *et al.* 1995; Cochran *et al.* 2003, 2006; Liu *et al.* 2004). Systematic analysis based on repeating earthquakes also found no observable temporal changes in SWS associated with the 1999 M_w7.1 Düzce (Peng & Ben-Zion 2005), the 1999 M_w7.6 Chi-Chi (Liu *et al.* 2005a), and the 2004 M_w6.0 Parkfield earthquake (Liu *et al.* 2008). Using a Accurately Controlled Routinely Operated Signal System (ACROSS) deployed along the Nojima fault zone that ruptured during the 1995 Kobe earthquake, Ikuta & Yamaoka (2004) found an abrupt increase and subsequent recovery in the traveltime of direct *S* waves associated with the 2000 M_w6.6 Western-Tottori earthquake (∼0.4 per cent), and the 2001 M_w6.4 Geiyo earthquake (∼0.1 per cent). The observed delays in the *S*-wave traveltimes were polarized in the direction perpendicular to the Nojima fault, indicating a slight increase of shear wave anisotropy in association with the nearby earthquakes. These results suggest that temporal changes in anisotropy caused by large earthquakes may be observable, although the amplitudes of the changes could be much smaller than those associated with direct measurements in seismic velocities.

In this study, we quantify temporal changes of seismic velocity and shear wave anisotropy in the shallow crust using local earthquakes recorded at a 200-m-deep borehole station CHY in Taiwan (Fig. 1). This station is located directly above the hypocentre of the 1999 October 22, *M*6.4 Chia-Yi earthquake, and has recorded many small earthquakes with clear surface reflected waves and SWS signals. Liu *et al.* (2004, 2005a,b) have systematically analysed the temporal changes of SWS and attenuation anisotropy at this station before and after the 1999 September 20 M_w7.6 Chi-Chi earthquake, and the *M*6.4 Chia-Yi earthquake occurred about 1 month later. They concluded that the SWS delay times and polarization directions of the fast waves do not show significant changes associated with the nearby large earthquakes. Our study is motivated by the results of Liu *et al.* (2004, 2005a), but differs from their work in the following aspects. First, Liu *et al.* (2004, 2005a) only measured the temporal changes in SWS delay time δt at station CHY. Here, we apply a similar technique to measure the time delay (TD) between the clear incident (upgoing) and surface-reflected (downgoing) signals, and quantify temporal changes in the direct *P* and *S* waves for both fast and slow components, as well as the SWS δt. In addition, we group the earthquakes into different clusters based on their locations and waveform similarities. We confirm that the obtained variations in the TDs are relatively insensitive to earthquake locations, but mostly reflect temporal changes of material properties in the top 200 m of the crust.

In the following sections, we first describe the analysed data and background information. In Sections 3 and 4, we outline the analysis procedure, and apply it to the entire data set and different groups according to their locations and waveform similarities. We also discuss the observed temporal changes before, during and after the occurrence of Chia-Yi earthquake. Finally, we compare our results with previous studies and offer possible mechanisms that would explain our observations.

2 DATA AND BACKGROUND INFORMATION

We use three-component seismograms recorded by the 200-m-deep (173 m below sea level) borehole station CHY, which belongs to
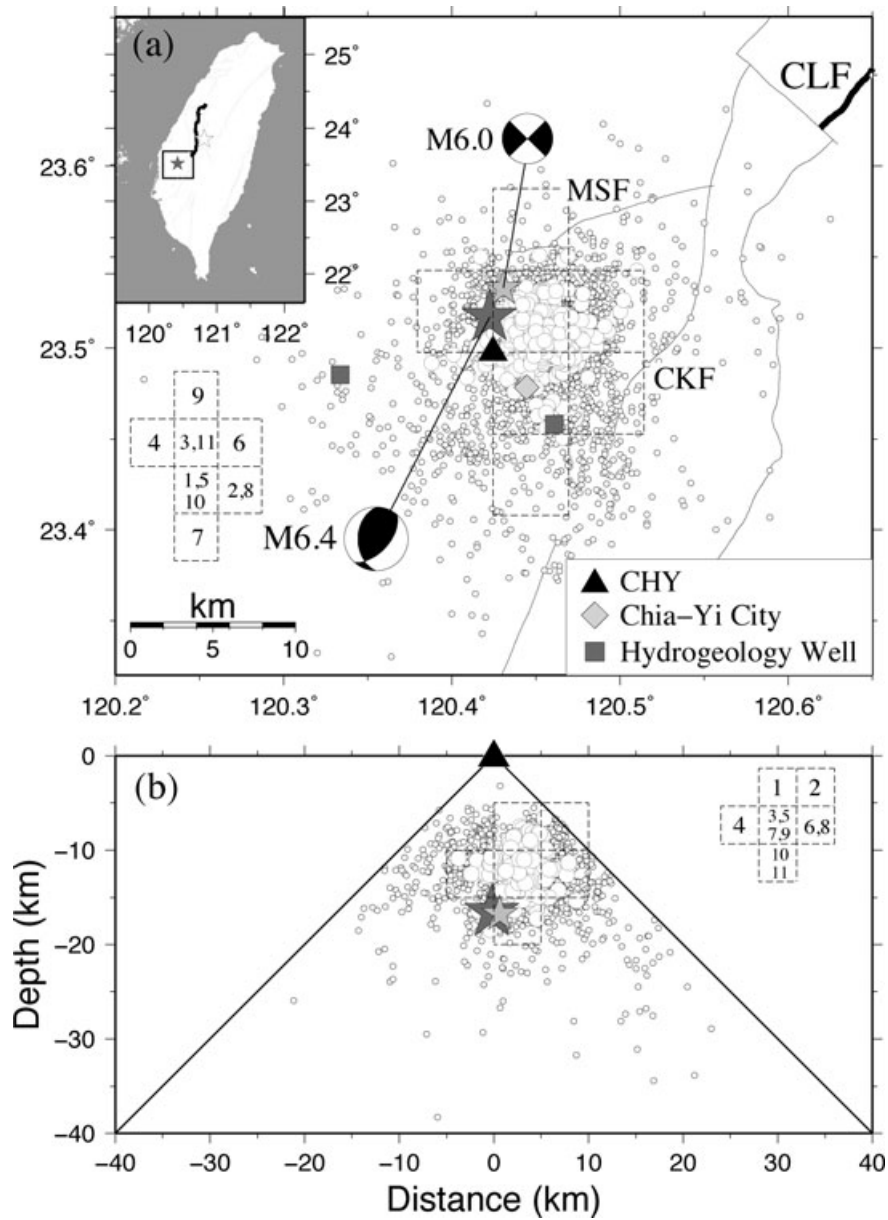
Figure 1. (a) The study area in central Taiwan. The black triangle marks the location of the 200-m-deep borehole station CHY, located at the outside of the Chia-Yi city (the diamond mark). Two stars denote the epicentre of the 1999 October 22 $M6.4$ Chia-Yi earthquake and the largest $M6.0$ aftershock, and the corresponding focal mechanisms are shown. The small circles mark the epicentre of earthquakes with straight-line incident angle less than $45°$. The large circles mark the locations of earthquakes belong with similar clusters with $\beta_c = 0.85$. The thin lines are the active faults, including Meishan fault (MSF) and Chukou fault (CKF) near Chia-Yi city. The numbers on the grid lines mark the locations of different cube cells shown in Fig. 6. The length of each cube cell is 5 km. The inset shows the map of Taiwan with the box corresponding to the study area. The white star marks the epicentre of the 1999 September 20 $M_w 7.6$ Chi-Chi earthquake and the bold line is the Chelungpu fault (CLF) ruptured during the Chi-Chi main shock. (b) The cross-section view below CHY. The grid lines and number mark the locations of the cube cells in cross-section view.

the Taiwan Central Weather Bureau Seismic Network (CWBSN). This network consists of 75 stations with S-13 1-Hz short-period velocity seismometers (Shin & Teng 2001). In addition, a free-field strong-motion station CHY073 is colocated with the borehole station, which belongs to the Taiwan Strong-Motion Instrumentation Program (TSMIP). In this study, we only analyse the weak-motion short-period seismic data recorded by the borehole seismometer CHY.

The site CHY is located at a flat plane outside the Chia-Yi city (Fig. 1) on the southwestern foothills of Taiwan (Hung *et al*. 1999).

Downhole drilling sample shows that the top 30 m contains mixture layer with silty sand and clays (Tai-Tech 2000). The average *S*-wave velocity in the top 30 m is $200\,\mathrm{m\,s^{-1}}$ (http://geo.ncree.org.tw/). This site is classified with class D, which represents stiff soils according to the 1997 Uniform Building Code (UBC) Provisions (Kuo 1994; Dobry *et al*. 2000; Lee *et al*. 2001; Chung 2006). However, the drilling sample in the depth range of 30 and 200 m in this site is not available. Therefore, we examine samples from two nearby hydrogeological drilling holes (i.e. squares as shown in Fig. 1) within 6 km from CHY from the Hydrogeology Data Bank by the Central
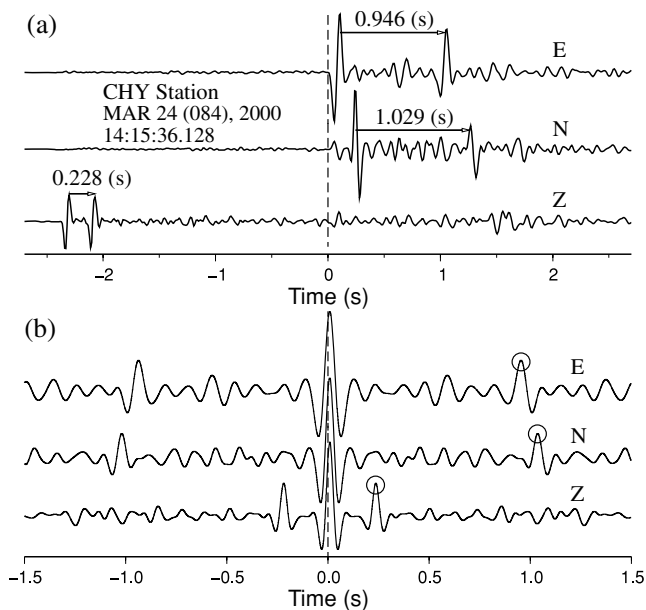
Figure 2. (a) An example of three-component seismograms showing the surface reflected waves and shear wave anisotropy. (b) The autocorrelation functions for the three-component seismograms. The dashed line corresponds to zero lag time and the open circles mark the secondary peaks, which is used as a proxy for the two-way traveltimes in the top 200 m.

Geological Survey of Taiwan (http://hydro.moeacgs.gov.tw/, in Chinese). The core samples show that the top 200 m of the crust around CHY mainly consists of fine- (0.125–0.25 mm) to coarse-grained (0.5–1.0 mm) sandstones, fine siltstones (0.004–0.063 mm) and mudstones (Liu *et al.* 2005b).

The 1999 October 22 *M*6.4 Chia-Yi earthquake occurred about 1 month after the 1999 September 20 M_w7.6 Chi-Chi earthquake (Chen *et al.* 2008; Wen *et al.* 2008). The main shock was located directly beneath the station CHY with a focal depth of 16 km, and was south of the Chelungpu fault (CLF) that ruptured during the Chi-Chi earthquake. The Chia-Yi earthquake was followed by a vigorous aftershock sequence, including one with *M*6.0 occurred 52 min after the main shock. The aftershocks outlined a blind-thrust fault that is dipping to the west at the depth range of 10–16 km (Chen *et al.* 2008).

3 ANALYSIS PROCEDURE

We select a total of ~2500 local earthquakes that occurred between 1991 March and 2002 March and are within the shear wave window of station CHY for further analysis (Nuttli 1961; Cochran *et al.* 2003; Peng & Ben-Zion 2004). The shear wave window is defined as the epicentral distances to station CHY less than their hypocentral depths (i.e. straight-line incident angle ≤45°). We manually pick the arrival times of *P* and *S* waves for all events, and only keep those with clear incident and surface reflect waves in three (N, E and Z) components (e.g. Fig. 2). Next, we cut the data 8 s before and 12 s after the *S*-wave arrival, remove the mean value, re-sample the data from 50 to 100 samples per second, and apply a 1 Hz high-pass filter to reduce the long-period background noise. We further eliminate bad quality events according to their signal-to-noise ratio (SNR). The signal window is between 0.5 s before and 1.5 s after the *P*-or *S*-wave arrival, and the noise window starts from 2.5 to 0.5 s before *P*-wave arrival. Any events with SNR ≤ 2.0 for any of the three components are not used for further analysis (~22 per cent of original events).

Fig. 2(a) shows an example of typical waveforms recorded by the borehole station CHY, which contain several interesting features. First, the *P* and *S* waves are most clearly shown in the vertical and two horizontal components, respectively, indicating a near-vertical incidence for the seismic waves. Second, clear surface reflected waves are observed on all three components with different time lags, corresponding to different traveltimes in the top 200 m. Finally, the *S* wave on the E component arrives about 0.16 s faster than that on the N component, indicating the presence of near-surface anisotropy in this area. Liu *et al.* (2004) measured SWS parameters in the same region, and found an average delay time δt of 0.16 s and a fast direction ϕ of 279.8° ± 4.1° (i.e. clockwise from north) from the borehole station CHY, and $\delta t = 0.20$ s, $\phi = 272.5° ± 4.3°$ from the surface station CHY073. Their results are generally consistent with the example shown here. We also measure the fast polarization directions for selected events and obtained similar directions. Because the fast direction is near E–W, and the obtained results remain essentially the same before and after rotating to the fast directions, we use waveforms recorded on the E component to represent the quasi-*S* waves corresponding to the fast direction in the following work.

Next, we compute the autocorrelations functions (ACF) for each of the three-component seismograms (Liu *et al.* 2004, 2005b), and measured the TD between the incoming (upgoing) and surface-reflected (downgoing) waves from the zero-lag and secondary peaks in the ACF (Fig. 2b). The underlying assumption is that for near-vertical incidence, the ACFs of the surface-reflected waves represent the Green's function for near-surface layers (e.g. Claerbout 1968; Daneshvar *et al.* 1995). This assumption is generally valid for small incident angles because seismic rays tend to bend towards near vertical, due to a reduction in seismic velocities in the near surface layers. In this case, the secondary peaks shown in the ACF (Fig. 2b) corresponds to the best match between the upgoing and downgoing waveforms (Fig. 2a), and the time between the zero-lag and secondary peaks in the ACF provides a good approximation of the two-way traveltimes in the shallow layers above the borehole station.

In detail, we cut the horizontal component data 1 s before and 3 s after the *S*-wave arrivals, and vertical component data 0.5 s before and 1 s after the *P*-wave arrivals. The time window is chosen to be long enough to include the both the direct and surface reflected waves (~0.94 to 1 s TD for the *S* wave, and ~0.22 s for the *P* wave), but short enough so that they do not contain both direct *P* and *S* waves. Then we measure the TD for the upgoing and downgoing *P* waves on the vertical component (Z), and *S* waves for the two horizontal components (N and E) from secondary peaks in the ACF. As shown in Fig. 2(b), the maximum peak is at zero lag and the secondary peak corresponds to the TD between the direct and surface-reflected phases. The ratio between the secondary and zero-lag peaks gives the cross-correlation coefficient between the direct and surface-reflected phases. We require that the ratio to be larger than 0.20 to ensure waveform similarity and reliability of the TD. This criterion results in additional dropping of 14 per cent of the data. Finally, we have a total of 1612 (~64 per cent of original events) high-quality events for further analysis. Out of them, 218 events occurred before and the rest 1394 events occurred after the Chia-Yi earthquake.
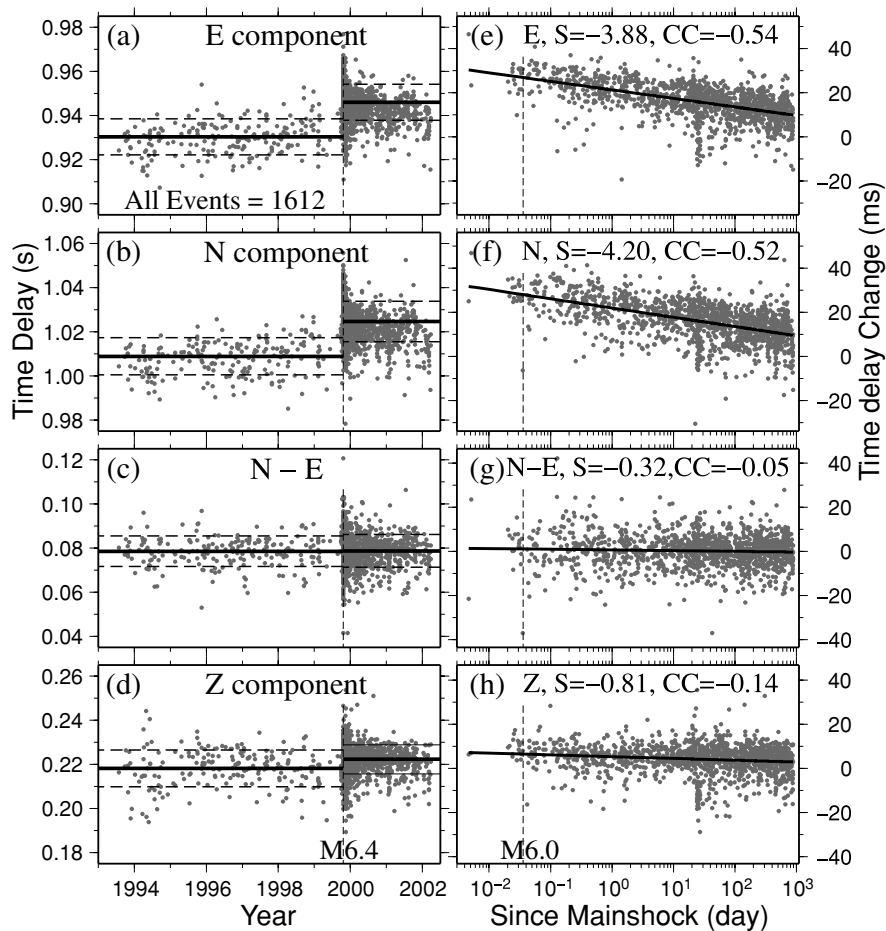
Figure 3. (a)–(d) Temporal changes of time delays (TDs) for the E, N, N–E and Z components versus the occurrence times of all 1612 events analysed in this study. The solid lines represent the mean TD before and after *M*6.4 Chia-Yi earthquake, and the standard deviations are marked as dotted lines. (e)–(h) Temporal changes of TD for all components plotted with logarithmic time (in days) since the Chia-Yi main shock. The solid line marks the least-squares fitting of the data. The vertical dashed line mark the occurrence of the *M*6.0 aftershock. The measured slope *S* (ms per decade change in time), and the correlation coefficient (CC) values are also shown on the top of each panel. Clear increases of TDs for the N (f) and E (e) components are shown at the time of Chia-Yi main shock, followed by a logarithmic-type recovery. In comparison, there is lack clear changes in the vertical (h) and N–E components (i.e. SWS δt).

4 RESULTS

4.1 General features

The TDs calculated from three-component seismograms for all 1612 events are shown in Fig. 3. The average TD between 1993 and 2002 is 0.944 ± 0.010 s in the E, 1.023 ± 0.010 s in the N, and 0.222 ± 0.007 s in the Z component, respectively. We also compute the average time difference between the N and E components, which is used the as a proxy for SWS delay time δt in the top 200 m. The obtained value is 0.079 ± 0.007 s, close to the two-way SWS δt of 0.08 s measured by Liu *et al.* (2004). Other general patterns include: (1) a clear increase of TD for the N and E components at the time of Chia-Yi main shock, followed by a logarithmic-type recovery; (2) a gradual increase of TD for the E and N components in the 7 yr prior to the main shock and (3) a lack of clear temporal changes for the differences of TDs between the N and E components (i.e. SWS δt) and the TD for the vertical component.

To further quantify the temporal changes in each component, especially during the co- and post-seismic period, we fit the TD versus logarithmic times since the main shock by a least-squares method, and compute the correlation coefficients (CC) between

them. The obtained slopes and the CC values for each component are shown in Fig. 3. We also use the Student's *t*-test (Wilks 2006) to compute the probability of occurrence by random chance for each component. If the calculated probability *p* is 0.05, the occurrence by chance is 5 per cent or the results are significant at the 95 per cent level. The statistical test confirms that the observed correlations for the N, E and Z components are statistically significant (with $p < 0.05$ per cent of occurrence by chance), but the correlation for the SWS δt is not (with 6.5 per cent of occurrence by chance).

The general patterns shown in Fig. 3 are observed using all earthquakes within the shear wave window. However, the obtained temporal changes could be affected by mixing the spatial variations with the underlying temporal changes (e.g. Liu *et al.* 2004, 2005b; Peng *et al.* 2005). To examine this further, we plot in Figs 4(a)–(d) the TDs for the E component versus several earthquake location parameters (event depth, epicentral distance, true incident angle and backazimuth). The true incident angle is computed from the particle motion of the *P* wave (see Appendix A for the detailed analysis procedure). As shown in Figs 1 and 4(a), most of the events (99.4 per cent) are located at 5–20 km depth. The depth and the backazimuth appear to be less correlated with the TD (with CC values of 0.17 and –0.24, and $p < 0.05$ per cent of occurrence by chance, respectively). However, the TD shows larger negative
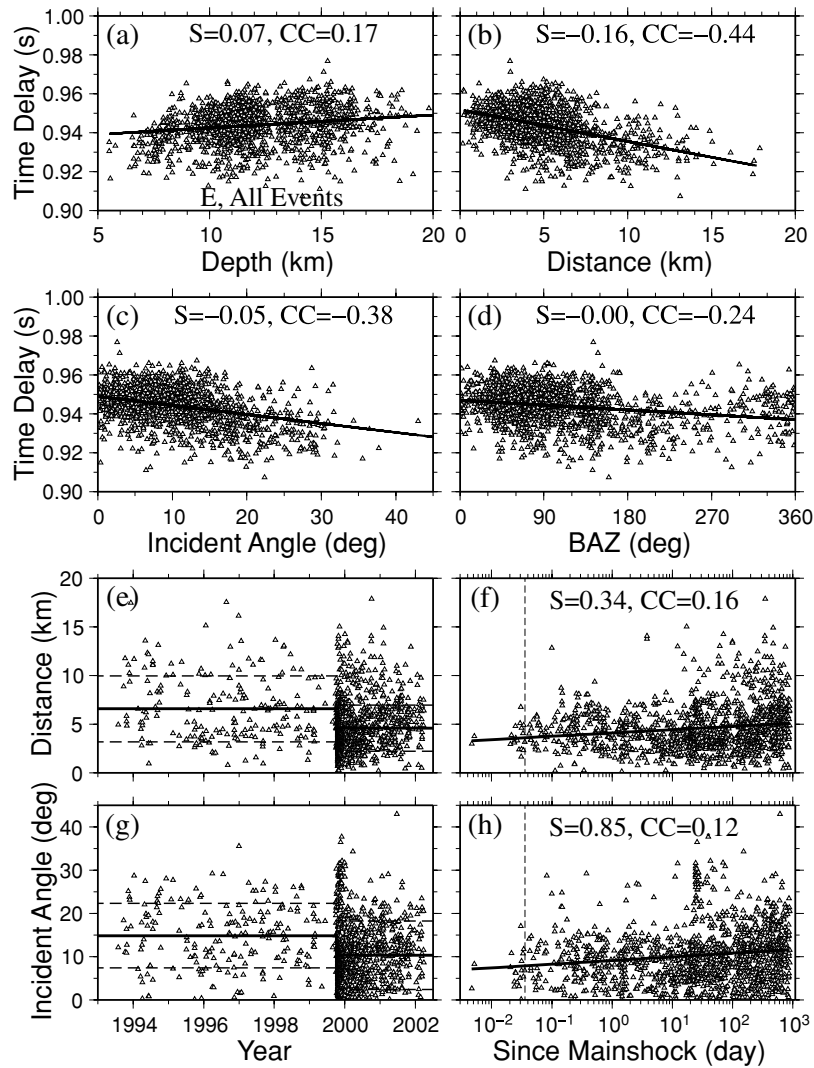
Figure 4. The TDs measured on the E component versus event depth (a), epicentral distance (b), true incident angle (c), and back azimuth (d) for all 1612 events. The epicentral distance versus the occurrence time (e) and logarithmic time since the Chia-Yi main shock (f). The true incident angle versus the occurrence time (g) and logarithmic time since the Chia-Yi main shock (h). Other symbols and notations are the same as in Fig. 3.

correlation with the increasing epicentral distance (CC = −0.44) and incident angle (CC = −0.38), with $p < 0.05$ per cent of occurrence by chance. This is mainly because for a homogenous medium, the total separation distances between the upgoing and surface reflected waves $\Delta s = 2d\cos(i)$, where d is the layer thickness and i is the incident angle (see Appendix B for the detailed mathematical derivation). Hence, the separation distances and the traveltimes between the upgoing and surface-reflected waves become smaller with increasing incident angles. Finally, the time evolutions of epicentral distances and true incident angles for all the earthquakes (Figs 4e–h) show a similar abrupt coseismic changes and post-seismic recovery as compared with those in Fig. 3. These results suggest that using earthquakes at different locations could potentially cause apparent temporal changes in the TDs. In the next two subsections, we will apply different techniques to group earthquakes into small clusters to reduce the effects of spatial variations on temporal changes.

4.2 Grouping by earthquake locations

First, we use 259 earthquakes that are within 3 km in radius to CHY and in the depth range of 10–15 km. Fig. 5 shows the observed

TDs for different components versus the logarithmic time and true incident angle after the main shock. The general patterns are similar to Fig. 3, but the scatter is somewhat reduced. In addition, because we only select earthquakes directly beneath station CHY, the true incident angles do not show significant dependence with TDs (i.e. Figs 5e–h). The results from using 1 to 2 km radius show similar patterns, although the numbers of events are reduced to 22 and 108, respectively.

Next, we group the 1612 events into small cube cells with 5 km in length and examine the TDs within each cube separately. All small cubes do not overlap with each other in space. We choose 5 km mainly based on the location error of the CWB catalogue, which is about 4 km in the study region (Wu & Teng 2002). It also reflects a trade-off between the need of small cube cells to remove spatial variations, and the need to have enough events for better statistics. We require that each group should contain at least 20 events and the time period is long enough to span from one day to 2 yr after the main shock. A total of 11 cube cells between 5 and 20 km in depth, and within 10 km in both E–W and N–S direction have been selected (see Table S1). Figs 6(a)–(d) show the measured slopes for different groups between the TDs and logarithmic times
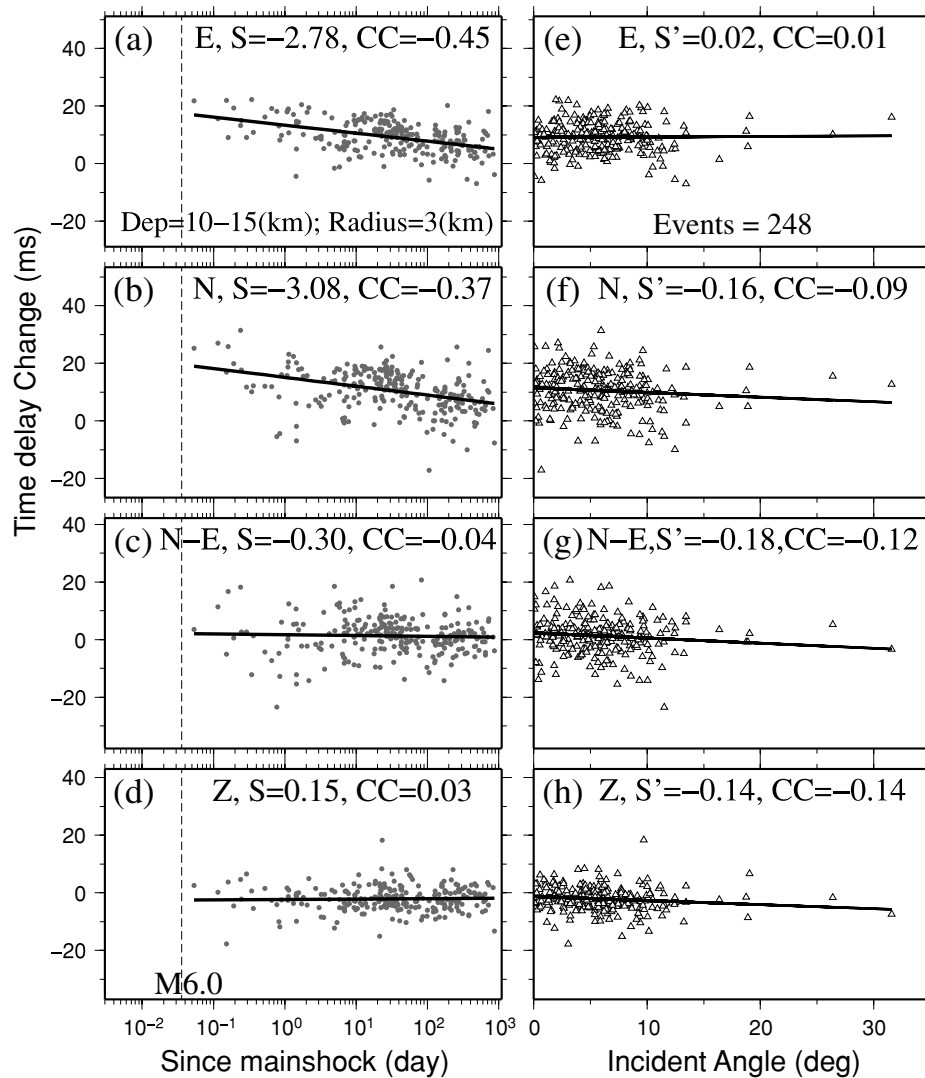
Figure 5. (a)–(d) Temporal changes of the TDs for all components plotted with logarithmic time (in days) since the Chia-Yi main shock for 248 events within 3 km of station CHY and in the depth of 10–15 km. (e)–(h) The TDs for all components versus the true incident angles since the Chia-Yi main shock. Other symbols and notations are the same as in Fig. 3.

since the main shock. It is clear that for all groups (Fig. 6e), the TD measured at the E and N components increase at the time of the main shock and recover gradually, but virtually no temporal changes are observed for the Z component and the time difference between N and E components (i.e. SWS δt). We also check the dependence on TDs on the true incident angle for each cube, and find no clear correlation among them (Fig. 6f).

4.3 Grouping by similar earthquake clusters

In the second approach, we group earthquakes into similar earthquake clusters by waveform cross-correlation (Aster & Scott 1993; Peng & Ben-Zion 2005) to minimize the mixing of spatial variations with temporal changes in our seismic data. The underlying assumption is that in a heterogeneous earth structure, only earthquakes in the nearby region generate similar waveforms (Menke & Schaff 2004; Peng & Ben-Zion 2005). In detail, we compute the waveform cross-correlations starting from 2 s before to 3 s after the arrival of S wave in E, N and Z components. Next, we compute median correlation coefficient (β) between event pairs with interhypocen-

tral distance less than 5 km. Finally, we identify pairs of events that satisfy a given similarity criterion ($\beta \geq \beta_c$) and group such pairs into similar earthquake clusters using an equivalency class (EC) algorithm (e.g. Press *et al.* 1986). The resulting number of clusters and total number of events within each cluster depend on the β_c value (e.g. Peng & Ben-Zion 2005). For example, the number of events in the largest cluster is 684, 340 and 188 with $\beta_c = 0.80$, 0.85 and 0.90, respectively. The events in the largest cluster with higher β_c (e.g. $\beta_c = 0.85$) are the subset of lower one (e.g. $\beta_c = 0.80$).

The obtained temporal changes in TD for the largest cluster with different choices of the β_c value are shown in Fig. 7. Fig. 8 shows the obtained ACF around the secondary peaks for three-component seismograms with $\beta_c = 0.85$. The overall patterns are very similar to each other, and are consistent with those shown in Figs 3 and 5(a)–(d). In addition, the correlation between the TD and the earthquake location is largely reduced (i.e. comparing Figs 9 and 4), suggesting again that the observed temporal changes are not mainly caused by spatial variations in the earthquake locations.
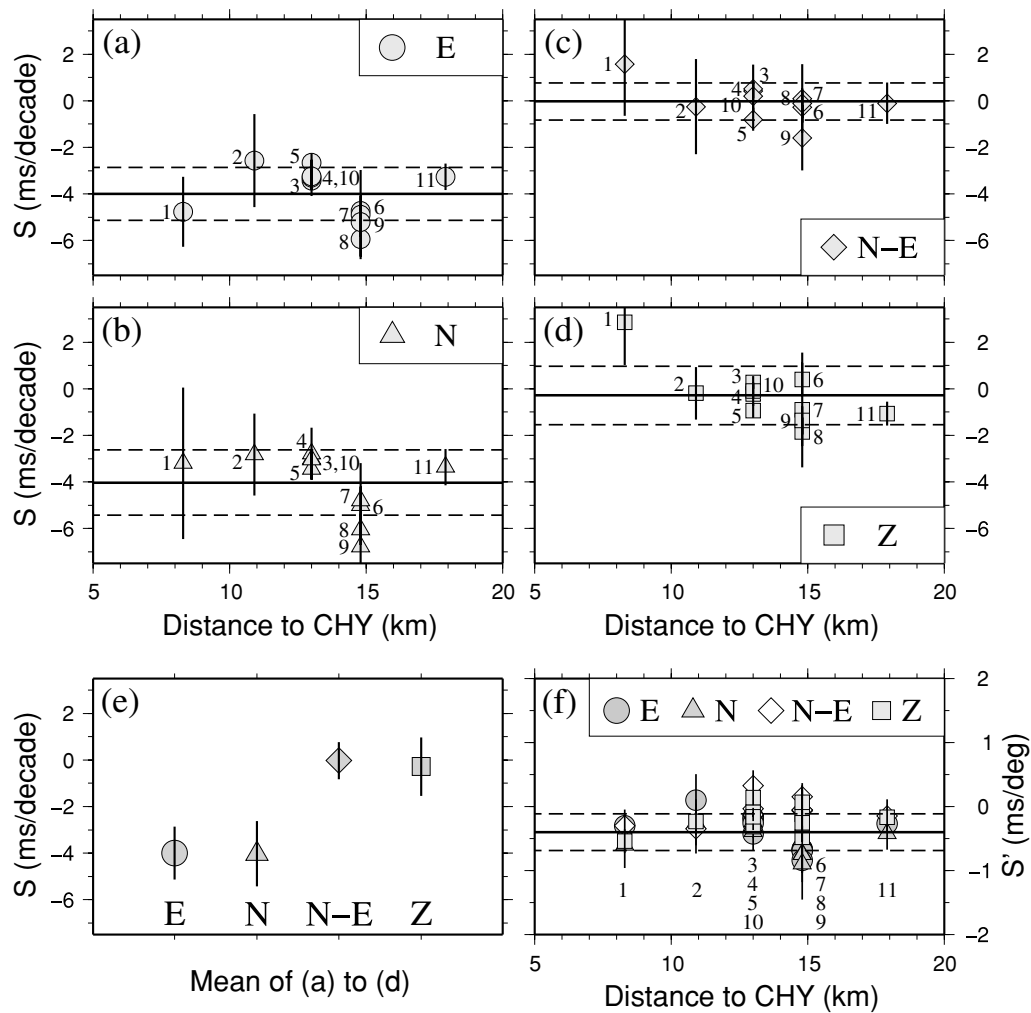
Figure 6. (a)–(d) The slopes (ms per decade) versus hypocentral distance (km) for all three components and the difference between N and E components measured from earthquakes grouped by their locations (cube cells shown in Fig. 1). The slope S (ms per decade) in vertical axis is calculated from the least-squares-fitting between the TDs and the logarithmic time since the Chia-Yi main shock. The horizontal axis represents the hypocentral distance (km) from the centre of each cube to CHY. The number from 1 to 11 represent different group of cube cells, and their corresponding locations are shown in Fig. 1 and listed in Table S1. The solid line marks the mean slope, and the dashed lines correspond to the one standard deviation of the mean. (e) Summary plot of mean slope of all 11 groups in different components from (a) to (d). (f) The slopes S' (ms deg^{-1}) between the TDs and the true incident angles since the main shock versus hypocentral distance (km) for all components and all 11 groups. The results presented in this figure show that the temporal changes observed at the N and E components are largely independent of the earthquake locations.

4.4 Pre-, co- and post-seismic temporal changes

Since the results from different choices of β_c are similar (Fig. 7), we calculate the co- and post-seismic changes in seismic velocities based on the measurements with $\beta_c = 0.85$. The average TD for each component before Chia-Yi main shock is used as a measure for pre-main shock level. Because the post-seismic changes is approximately linear in logarithmic time, we fit the data by a least-squares procedure using a logarithmic relation (Peng & Ben-Zion 2006)

$$\text{TD}(t) = a - b \log_{10}(t \text{ day}^{-1}), \tag{1}$$

where a is the TD in ms at 1 day after the main shock, b is a measure of the decreasing rate of the TD per decade change in time. The parameter a is associated with initial conditions, and the parameter b represents the healing rate, which is the speed for material to recover to the undamaged status (e.g. Lyakhovsky *et al.* 1997, 2005). We note that this equation is valid for finite positive times because it diverges as t approaches 0 or infinity. The coseismic change is

measured as the difference between the extrapolated TD at 1 hr after the main shock (i.e. ~8 min after the M6.0 aftershock) and the averaged TD before the main shock. We choose 1 hr because it is close to the starting time of the first valid measurement after the main shock. The actual coseismic and early post-seismic changes could be much larger (e.g. Sawazaki *et al.* 2006, 2009; Karabulut & Bouchon 2007; Wu *et al.* 2009a, 2009b), but we do not have valid data point during and immediately after the main shock to provide further constraints. Hence, the coseismic changes reported below should be considered as lower bounds.

As shown in Fig. 7, the TDs with $\beta_c = 0.85$ (i.e. blue symbols) for the E (fast S) and N (slow S) components increase coseismically from 0.938 to 0.950 s and from 1.016 to 1.037 s, respectively (also see Table S1 for the detailed values). The TD in the Z component (P wave) drops coseismically from 0.225 to 0.224 s. The SWS δt decreases coseismically from 78.35 to 77.95 ms. If we assume that the ray paths in the top 200 m of shallow crust remains unchanged before and after the main shock, we can directly convert the
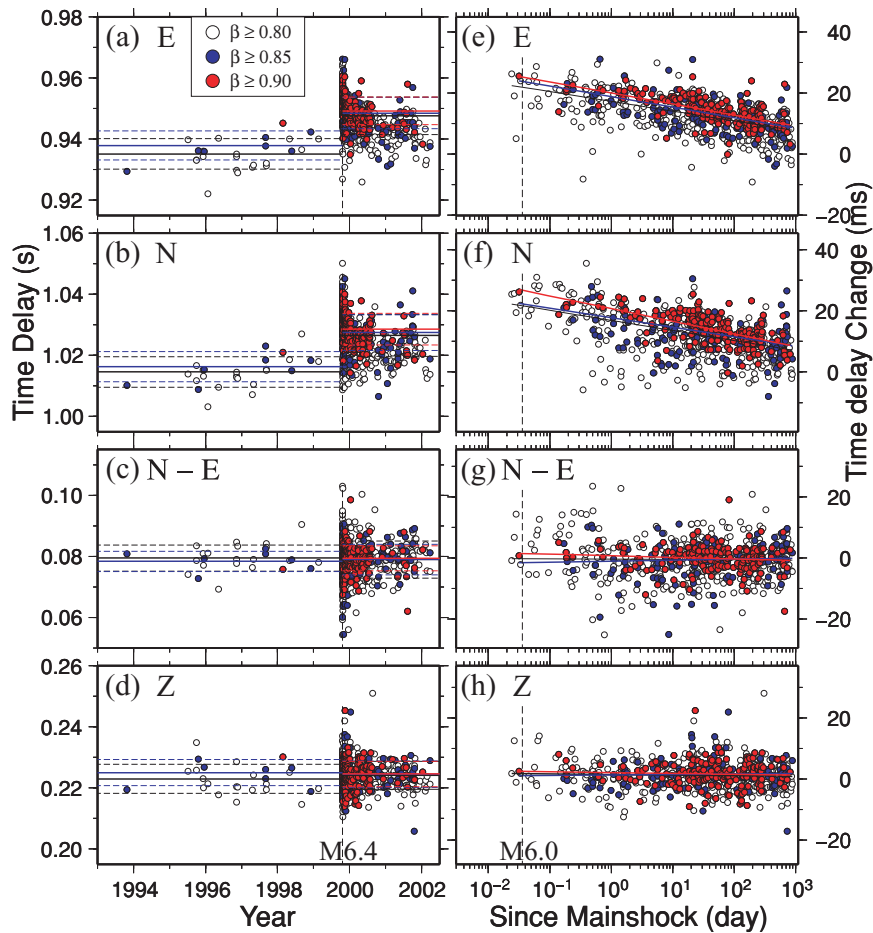
Figure 7. (a)–(d) Temporal changes of time delays (TDs) for the E, N, N–E and Z components versus the occurrence times of 684, 340 and 180 events in the largest similar earthquake cluster with $\beta_c = 0.80$ (white circle), 0.85 (blue circle) and 0.90 (red circle), respectively. (e)–(h) TDs change versus logarithmic time (in days) since the Chia-Yi main shock. The percentage of coseismic changes are given in online Table S1. Other symbols and notations are the same as in Fig. 3. The observed patterns of temporal changes are also similar to those shown in Fig. 3.

measured TD into traveltime changes in *P*- and *S*-wave velocities by dividing the two-way travel distance of 400 m. The obtained *P*, fast and slow *S* waves before the main shock are 1781.6, 421.8 and 389.4 m s^{-1}, respectively. The magnitude of the SWS (defined as the difference in the speed of fast and slow waves divided by their average) in the top 200 m is ∼8 per cent. The corresponding coseismic velocity changes in the fast *S*, slow *S*, *P* and magnitude of SWS is 1.28, 2.02, 0.44 and 0.51 per cent, respectively (e.g. Fig. 7). As noted before, the small coseismic changes in the *P* waves and SWS δt are not statistically significant. The healing rates of TD in E and N component are 3.45 and 3.12 ms per decade changes in time after the main shock, respectively. We note that about 27 months (i.e. 2002 March) after the main shock, the TD still does not return to the average value before the main shock, suggesting either a relatively long recovery process, or permanent changes in the shallow crust (e.g. Schaff & Beroza 2004).

We also examine the data in the 7 yr prior to the Chia-Yi main shock, and find a gradual increase of TDs for both the fast and slow *S* waves. Such changes are shown both in the entire data set with relatively large scatters (Figs 10a–d), and the similar earthquake clusters with relatively small number of observations (Figs 10e–f). The least-squares fitting to the data with $\beta_c = 0.85$ shows that the TD increases 2.29 and 2.09 ms yr^{-1} in E and N components, respectively. The changes for SWS δt and the Z components as

shown in Figs 10(g) and (h) are –0.21 and 0.3 ms yr^{-1}, respectively, much smaller than the values for the E and N components.

5   DISCUSSIONS

In this study, we utilized surface-reflected *P* and *S* waves to quantify temporal changes of *P*- and *S*-wave velocities, and shear wave anisotropy in the top 200 m of the shallow crust associated with the occurrence of the 1999 *M*6.4 Chia-Yi earthquake. We found clear coseismic increases of TD for the *S* waves on the E (fast) and N (slow) components (on the order of 1–2 per cent), followed by the logarithmic recovery (e.g. Figs 3, 5 and 7–8). In contrast, the variations for the *P*-wave velocity on the vertical component and the SWS delay time δt are less than 1 per cent and not statistically significant (e.g. Figs 7g and h). We also find a gradual increase of TD on the E and N components (i.e. decrease of *S*-wave velocity) in the 7 yr prior to the Chia-Yi main shock, and no clear changes on the Z component and the SWS δt (e.g. Fig. 10).

Several factors can cause the temporal changes observed in this study. These include changing earthquake locations and ray paths, and variations in the elastic properties of the medium. As shown in Fig. 4 and Appendix B, a systematic decrease of true incident angles (Fig. 4c) or epicentral distance (Fig. 4b) produces an apparent
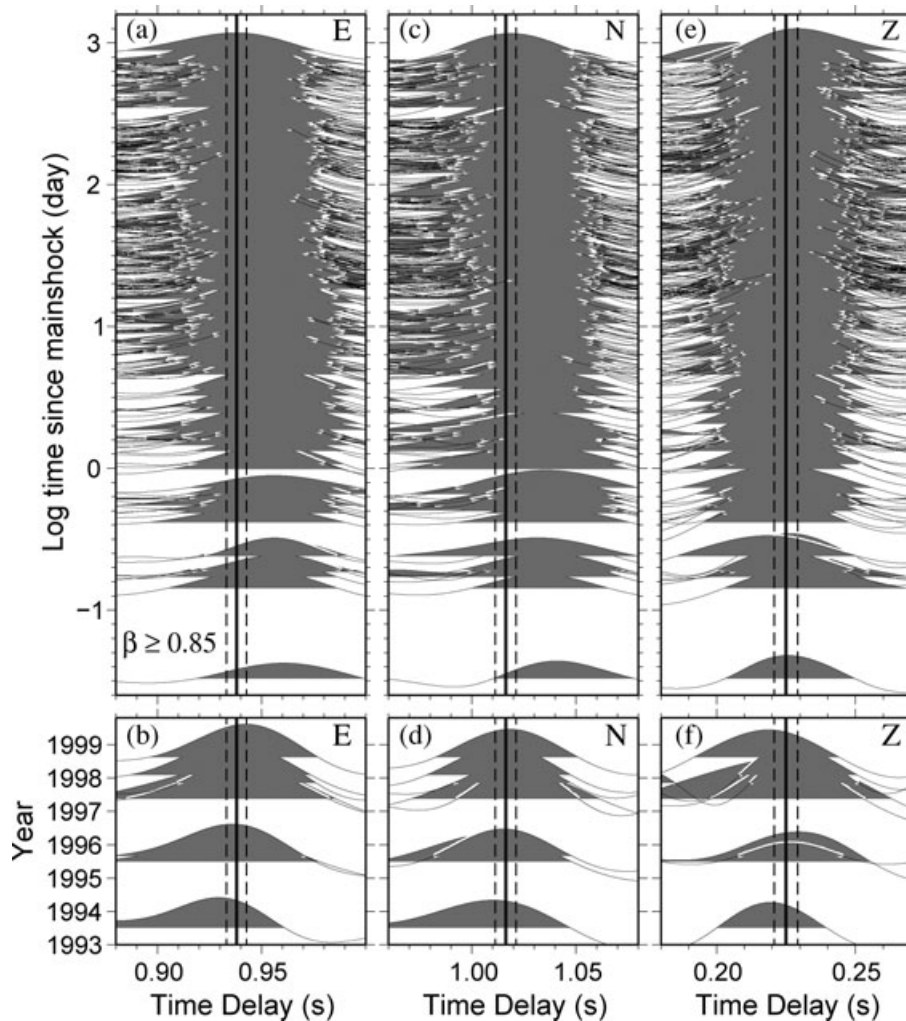
Figure 8. Autocorrelation functions (ACF) in E (a, b), N (c, d) and Z (e, f) components for 340 similar earthquakes with $\beta_c = 0.85$. The lower panel shows the ACF versus the occurrence time before the main shock. The upper panel shows the ACF versus logarithmic time since Chia-Yi main shock. The vertical solid line marks the average TD before the main shock, and the standard deviation are marked as dotted lines, which are 0.9379 ± 0.0048 s in the E component, 1.0163 ± 0.0049 s in the N component, and 0.2250 ± 0.0042 s in the Z component. The corresponding coseismic velocity changes in E, N and Z components is 1.28, 2.02 and 0.44 per cent, respectively.

increase of TD observed in this study. However, we observe similar patterns as shown in Fig. 3 for the entire data set by grouping the earthquakes into small clusters based on their locations and waveform similarities (Figs 5–8). In addition, the dependences of the observed TDs with earthquake locations are largely reduced (i.e. comparing Figs 9 to 4). These results suggest that changing earthquake locations could contribute to the observed scatter, but are not the primary reason for the observed temporal changes. This is perhaps not too surprising because, as mentioned before, seismic rays tend to bend towards vertical due to a reduction in seismic velocities in the near surface layers. So the dependence on the ray paths of the incoming waves is rather weak, especially for earthquakes with small epicentral distances (Fig. 5). This is also consistent with the fact that virtually no *P*-wave energy is shown on the horizontal, and no *S*-wave energy is shown on the vertical components for majority of the events (Fig. 2). Based on these observations, we suggest that the observed temporal changes in the TDs are mainly caused by temporal changes in the medium, rather than spatial variations in the earthquake locations. Because the surface reflected waves only sample the top 200 m of the crust, we attribute the observed

temporal changes in TDs to variations of elastic properties in the near-surface layers.

We propose that physical damage in near-surface layers caused by the strong ground motions of nearby large earthquakes (e.g. Rubinstein & Beroza 2004a,b, 2005; Schaff & Beroza 2004; Peng & Ben-Zion 2006; Ma 2008; Zhao & Peng 2009) is the main cause of the temporal changes in elastic and anisotropic properties observed in this study (Fig. 11). During the Chia-Yi main shock and subsequent large aftershocks, the strong ground motions cause an abrupt increase of crack and void densities, which could be generated by opening and growth of pre-existing fractures and increase of porosity in the shallow surface layers. After the main shock, normal stresses from lithostatic loadings would close the coseismically opened cracks and increase the packing of shallow sediments, resulting in a recovery of seismic velocity to the pre-main shock level in log-linear fashion. Similar logarithmic healing processes have been observed in laboratory experiments with granular material and rocks under normal stresses (e.g. Dieterich & Kilgore 1996; Marone 1998; TenCate *et al.* 2000; Scholz 2002; Johnson & Jia 2005; Johnson & Sutin 2005).
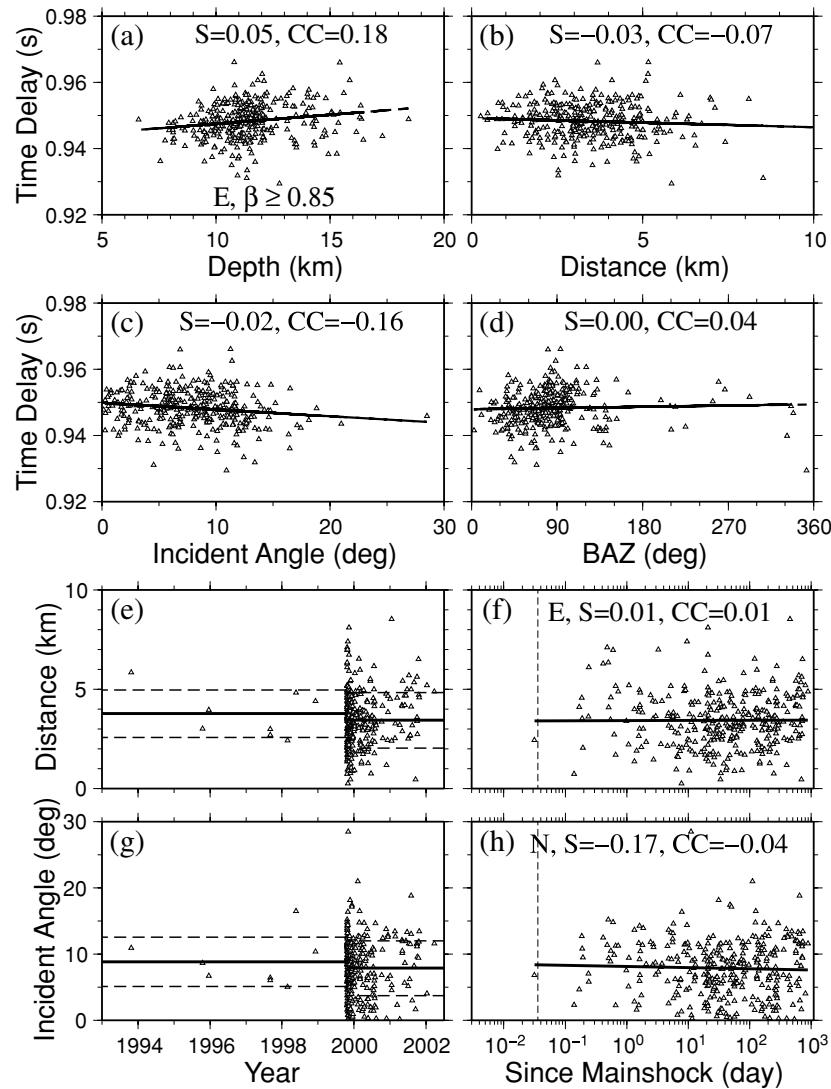
Figure 9. The TDs measured on the E component versus event depth (a), epicentral distance (b), true incident angle (c), and back azimuth and (d) for the 340 similar earthquakes with $\beta_c = 0.85$. The epicentral distance versus the occurrence time (e) and logarithmic time since the Chia-Yi main shock (f). The true incident angle versus the occurrence time (g) and logarithmic time since the Chia-Yi main shock (h). Other symbols and notations are the same as in Fig. 4.

Because the fast *S*-wave polarization direction is parallel to the E–W maximum horizontal compressive stress (e.g. Liu *et al.* 2004, 2005a,b), as inferred from the *P*-axis based on the focal mechanism of Chia-Yi main shock (Chan & Ma 2004) and the regional GPS velocity field (Yu *et al.* 2001), we suggest that preferential alignment of the fluid-filled fractures and microcracks to the direction of the maximum horizontal compressive stress is the main cause of the observed shear wave anisotropy. Fractures with other orientations could also exist but they are likely closed by the E–W maximum horizontal compressive stress (e.g. Boness & Zoback 2006). Because we observed clear changes in both fast and slow *S*-wave velocities and no resolvable changes in SWS δt, we infer that the coseismic increase of crack and void densities do not have a preferred orientation. In addition, we observed no clear temporal changes in the *P*-wave velocities. Previous studies have shown that *S*-wave velocities change much more than *P*-wave velocities when fluids is present (e.g. Mavko *et al.* 1998). The water table from measurements within 20 km of station CHY is in the range of 2–15 m (http://gweb.wra.gov.tw/wrweb). Hence, we suggest that the cracks and void spaces are fluid-filled. This is compatible with a very

large *Vp/Vs* ratio of 4.4, and a Poission's ratio of 0.47 in the study region.

Our results are generally consistent with previous studies based on waveform analysis of repeating earthquakes and artificial sources. These studies generally show clear coseismic reduction of *S*-wave velocities on the order of a few per cent in the shallow crust and near active fault zones (e.g. Schaff & Beroza 2004; Rubinstein & Beroza 2004a,b, 2005; Peng & Ben-Zion 2006; Li *et al.* 2006; Rubinstein *et al.* 2007), a smaller change in *P*-wave velocities (e.g. Schaff & Beroza 2004), and a lack of clear coseismic changes in shear wave anisotropy (e.g. Liu *et al.* 2004, 2005a, 2008; Peng & Ben-Zion 2005; Cochran *et al.* 2006) associated with large nearby earthquakes. It is worth noting that small temporal changes in shear wave anisotropy has been observed using the ACROSS (Ikuta & Yamaoka 2004). Such changes, even if exist, may not be clearly observable using the current technique, probably because of mixing of earthquakes with slightly different ray paths. Hence, we suggest that direct measurements of time variations in the direct *S*- and *S*-coda waves, as well as surface reflected *S* waves, may provide a more promising tool than the SWS
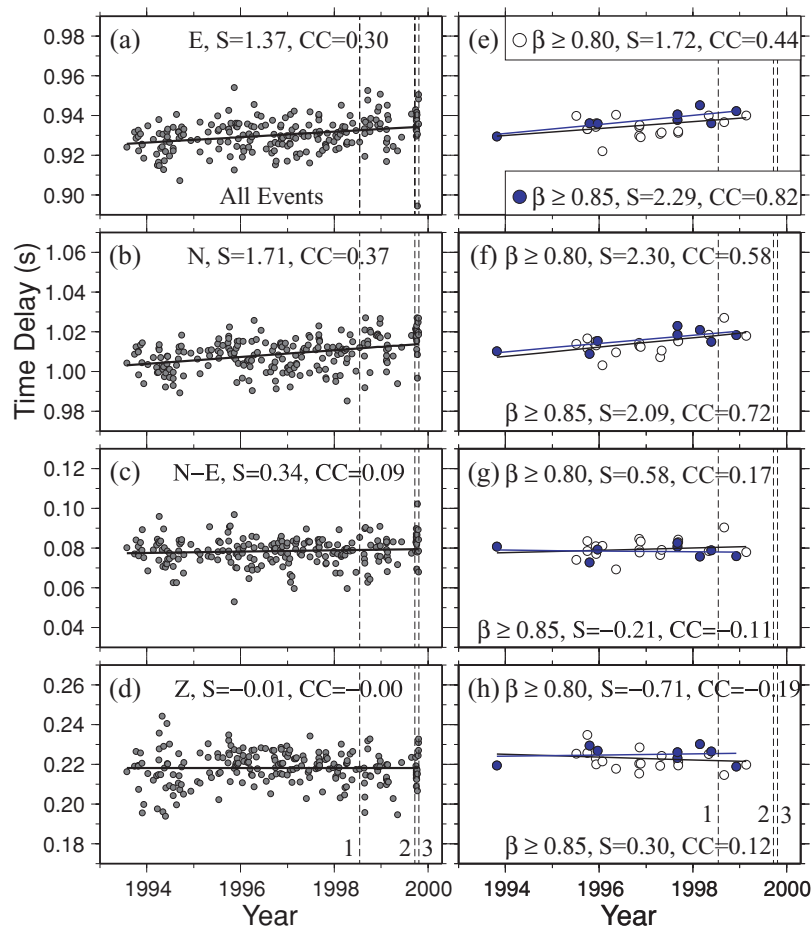
Figure 10. (a)–(d) Temporal changes of TDs for the E, N, N–E and Z components versus the occurrence times of all 218 events before the main shock. (e)–(h) Temporal changes of TDs of 26 and 8 events before the main shock for $\beta_c = 0.80$ (open circles) and $\beta_c = 0.85$ (blue circles), respectively. The vertical dotted lines 1, 2 and 3 mark the 1998 July 17 M6.2 Ruey-Li (i.e. epicentre located at ~25 km northeast of Chia-Yi city), 1999 September 20 M_w7.6 Chi-Chi, and 1999 October 22 M6.4 Chia-Yi earthquakes, respectively. A gradual increase of TDs for the E and N components in the 7 yr prior to the main shock are shown. In comparison, the temporal changes for the N–E and Z components are not clear.
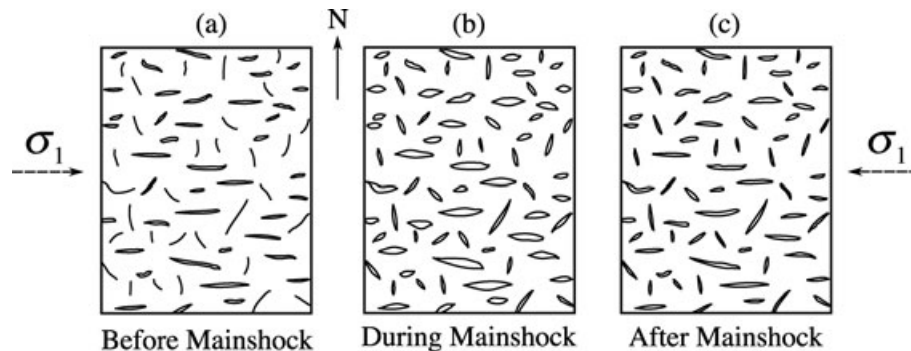
Figure 11. Schematic cartoon demonstrating possible mechanism for the observed temporal changes in the shallow crust before (a), during (b) and after (c) the Chia-Yi earthquake.

signals for monitoring temporal changes in the upper crust (Peng & Ben-Zion 2006).

Other recent studies using spectral ratio techniques, which involve comparisons of weak and strong-motion responses based on the spectral ratio between a target and a reference site, have found much larger (on the order of 20–40 per cent) changes in seismic velocities in the shallow crust and inside active fault zones (e.g. Sawazaki *et al.* 2006, 2009; Karabulut & Bouchon

2007; Wu *et al.* 2009a,b). The difference in the observed co-seismic change is mainly caused by the fact that this work and previous studies of repeating earthquakes are based on waveform analysis of weak motion data, while the spectral ratio technique can be applied to the strong motion data recorded during and in the first few min/hr immediately after the main shock, when the recorded weak motion data are mostly off-scale. Hence, the spectral ratio technique can obtain the large coseismic and very early

post-seismic changes that are otherwise not observable by the other techniques.

Nevertheless, these observations are compatible with the widespread non-linear site response in the shallow crust during strong ground motion of moderate to large earthquakes (e.g. Beresnev & Wen 1996; Field *et al.* 1997; Rubinstein & Beroza 2004a). Many studies also found that large earthquakes could induce hydrological responses (e.g. changes of water table, surface water flows) and eruptions of volcanoes and geysers from near field to teleseismic distance (e.g. Rojstaczer *et al.* 1995; Brodsky *et al.* 2003; Jónsson *et al.* 2003; Wang *et al.* 2004; Elkhoury *et al.* 2006; Manga & Brodsky 2006; Manga & Wang 2007; Wang & Chia 2008; Wang *et al.* 2009). For example, Rojstaczer *et al.* (1995) and Wang *et al.* (2004) documented clear increase of streamflows following the occurrence of the 1989 $M_w 6.9$ Loma Prieta and the 1999 $M_w 7.6$ Chi-Chi earthquakes. Rubinstein & Beroza (2004a) suggested that the observed coseismic increase of streamflow and the coseismic decrease of seismic velocity are likely caused by the same mechanism. That is, strong shaking from nearby earthquakes may cause an transient increase of crack density and porosity, which leads to an increase of permeability and streamflows, as well as a reduction of the bulk and shear modulus and the seismic velocity. Recently, Ma (2008) performed 3-D dynamic rupture simulations incorporating a yielding criterion in the upper crust. The simulation results suggest that widespread near-surface damages are mainly caused by strong seismic waves, and a 'flower-like' damage zone at depth is mainly induced by dynamic stresses associated with the rupture front, consistent with our field observations.

Finally, we discuss the observed temporal changes before and after the main shock in the context of previous studies in the same region. As summarized in the introduction, there has been a long debate on whether SWS parameters can be used to detect temporal changes of fault zone properties, and stress-forecast future damaging earthquakes (e.g. Crampin *et al.* 1990, 1991, 1999, 2004; Aster *et al.* 1990; Aster & Shearer 1991a,b; Liu *et al.* 2004, 2005a; Seher & Main 2004; Crampin & Gao 2005). In particular, Liu *et al.* (2004) have systematically measured hundreds of SWS parameters at the same borehole station CHY and the surface station CHY073, and found no clear temporal changes in SWS δt before the 1999 Chi-Chi and Chia-Yi main shocks. On the other hand, based on the same measurements, Crampin & Gao (2005) identified a gradual increase of SWS δt several years prior to, and a decrease of δt in the last ~130 days immediately before the Chi-Chi main shock. Liu *et al.* (2005a) suggested that precusory patterns observed by Crampin & Gao (2005) are likely dominated by spatial rather than temporal variations of material properties.

In this study, we found that the observed temporal changes in the SWS δt and the *P*-wave velocities are very small and likely not statistically significant. Our results are largely consistent with the results of Liu *et al.* (2004, 2005a) on a lack of systematic changes in SWS δt associated with the Chi-Chi and Chia-Yi earthquakes. However, it is worth noting that the debates between Liu *et al.* (2004, 2005a) and Crampin & Gao (2005) mainly focused on the SWS measurements from the direct *S* waves at the CHY station. In other words, their SWS measurements sample the crust below 200 m, while in this study we focuses on the temporal changes in anisotropy and seismic velocities within the top 200 m.

As discussed before, we did find an abrupt coseismic increase (Figs 3, 5 and 7), a logarithemic post-seismic recovery (Figs 3, 5 and 7), and a gradual increase of TD for both the fast and slow *S* waves in the 7 yr prior to the Chia-Yi main shock (Fig. 10). The co- and post-seismic changes can be well explained by temporal changes in the

material properties in the shallow crust induced by strong ground motions of nearby large earthquakes. The underlying mechanism of the pre-seismic changes is still not clear. One posssible mechanism is that the E–W maximum horizontal compressive stress in this region gradually increases before the occurrence of the 1998 $M6.2$ Ruey-Li (Wu *et al.* 2003), 1999 Chi-Chi and Chia-Yi earthquakes. If so, this would result in opening of microcracks preferentially in the E–W direction and an increase in shear wave anisotropy (e.g. Crampin *et al.* 1999; Crampin & Gao 2005). In other words, if the orientations of the opened microcracks prior to these main shocks were in the E–W direction, we would expect to see an decrease of seismic velocities only in N component, rather than in both E and N components. However, we found gradual increases of TD in both E and N components, and the observed temporal changes in the SWS δt before the main shock are not statistically significant (Fig. 10c). Hence, the observation is not consistent with the hypothesis on stress built-up before the main shock. Instead, we suspect that the pre-seismic temporal changes (i.e. velocity decreases) are most likely caused by variations of water table, sediment packing or other surficial processes. Due to a lack of additional information about this site, we leave this question open for future studies.

REFERENCES

Aster, R.C. & Scott, J., 1993. Comprehensive characterization of waveform similarity in microearthquake data sets, *Bull. seism. Soc. Am.,* **83,** 1307–1314.

Aster, R.C. & Shearer, P.M., 1991a. High-frequency borehole seismograms recorded in the San Jacinto Fault Zone, Southern California, Part 1. Polarizations, *Bull. seism. Soc. Am.,* **81,** 1057–1080.

Aster, R.C. & Shearer, P.M., 1991b. High-frequency borehole seismograms recorded in the San Jacinto Fault Zone, Southern California, Part 2. Attenuation and site effects, *Bull. seism. Soc. Am.,* **81,** 1081–1100.

Aster, R.C., Shearer, P.M. & Berger, J., 1990. Quantitative measurements of shear wave polarizations at the Anza seismic network, southern California: implications for shear-wave splitting and earthquake prediction, *J. geophys. Res.,* **95,** 12 449–12 473.

Aster, R.C., Shearer, P.M. & Berger, J., 1991. Comments on "Quantitative measurements of shear-wave polarization at the Anza seismic network, Southern California: implications for shear-wave splitting and earthquake prediction by Aster, R.C., Shearer, P.M. & Berger J."–Reply, *J. geophys. Res.,* **96,** 6415–6419.

Beresnev, I.A. & Wen, K.-L., 1996. Review: Nonlinear soil response–a reality, *Bull. seism. Soc. Am.,* **86,** 1964–1978.

Beroza, G.C., Cole, A.T. & Ellsworth, W.L., 1995. Stability of coda wave attenuation during the Loma Prieta, California, earthquake sequence, *J. geophys. Res.,* **100,** 3977–3987.

Boness, N.L. & Zoback, M.D., 2004. Stress-induced seismic velocity anisotropy and physical properties in the SAFOD Pilot Hole in Parkfield, CA, *Geophys. Res. Lett.,* **31,** L15S17, doi:10.1029/2003GL019020.

Boness, N.L. & Zoback, M.D., 2006. Mapping stress and structurally controlled crustal shear velocity anisotropy in California, *Geology,* **34**(10), 825–828, doi:10.1130/G22309.1x.

Brodsky, E.E., Roeloffs, E., Woodcock, D., Gall, I. & Manga, M., 2003. A mechanism for sustained ground water pressure changes induced by distant earthquakes, *J. geophys. Res.,* **108,** doi:10.1029/2002JB002321.

Chan, C.H. & Ma, K.-F., 2004. Possibility of forecasting aftershock distributions from stress change: a case study of inland Taiwan earthquakes, *TAO,* **15,** 503–521.

Chen, Y.-G. *et al*., 2008. New seismogenic source and deep structures revealed by the 1999 Chia-yi earthquake sequence in southwestern Taiwan, *Geophys. J. Int.,* **172,** 1049–1054.

Chung, J.-K., 2006. Prediction of peak ground acceleration in southwestern Taiwan as revealed by analysis of CHY array data, *TAO,* **17**(1), 139–167.

Claerbout, J.F., 1968. Synthesis of a layered medium from its acoustic transmission Response, *Geophysics,* **33,** 264–269.

Cochran, E.S., Vidale, J.E. & Li, Y.-G., 2003. Near-fault anisotropy following the Hector Mine earthquake, *J. geophys. Res.,* **108,** 2436, doi:10.1029/2002JB002352.

Cochran, E.S., Li, Y.-G. & Vidale, J.E., 2006. Anisotropy in the shallow crust observed around the San Andreas Fault before and after the 2004 M 6.0 Parkfeld earthquake, *Bull. seism. Soc. Am.,* **96**(4B), S364–S375.

Coutant, O., 1996. Observation of shallow anisotropy on local earthquake records at the Garner Valley, southern California, downhole array, *Bull. seism. Soc. Am.,* **86**(2), 477–488.

Crampin, S., 1987. Geological and industrial implications of extensive-dilatancy anisotropy, *Nature,* **328,** 491–496.

Crampin, S. & Gao, Y., 2005. Comment on "Systematic analysis of shear-wave splitting in the aftershock zone of the 1999 Chi-Chi, Taiwan, earthquake: shallow crustal anisotropy and lack of precursory changes" by Yunfeng Liu, Ta-Liang Teng, and Yehuda Ben-Zion, *Bull. seism. Soc. Am.,* **95,** 354–360.

Crampin, S. & Zatsepin, S.V., 1997. Modelling the compliance of crustal rock—II. Response to temporal changes before earthquakes, *Geophys. J. Int.,* **129,** 495–506.

Crampin, S., Booth, D.C., Evans, R., Peacock, S. & Fletcher, J.B., 1990. Change in shear-wave splitting at Anza near the time of the North Palm Springs earthquake, *J. geophys. Res.,* **95,** 11 197–11 212.

Crampin, S., Booth, D.C., Evans, R., Peacock, S. & Fletcher, J.B., 1991. Comment on "Quantitative measurements of shear-wave polarizations at the Anza seismic network, Southern California: Implications for shear-wave splitting and earthquake prediction" by Aster, R.C., Shearer, P.M., and Berger, J., *J. geophys. Res.,* **96,** 6403–6414.

Crampin, S., Volti, T. & Stefansson, R., 1999. A successfully stress-forecast earthquake, *Geophys. J. Int.,* **138,** F1–F5.

Crampin, S., Volti, T. & Stefansson, R., 2004. Response to "A statistical evaluation of a 'stress-forecast' earthquake" by T. Seher & I. G. Main, *Geophys. J. Int.,* **157,** 194–199.

Daley, T.M. & McEvilly, T.V., 1990. Shear wave anisotropy in the Parkfield Varian Well VSP, *Bull. seism. Soc. Am.,* **80**(4), 857–869.

Daneshvar, M.R., Clay, C.S. & Savage, M.K., 1995. Passive seismic imaging using microearthquakes, *Geophysics,* **60,** 1178–1186.

Del Pezzo, E., Bianco, F., Petrosino, S. & Saccorotti, G., 2004. Changes in the coda decay rate and shear-wave splitting parameters associated with seismic swarms at Mt. Vesuvius, Italy, *Bull. seism. Soc. Am.* **94,** 439–452.

Dieterich, J.H. & Kilgore, B.D., 1996. Imaging surface contacts: power law contact distributions and contact stresses in quarts, calcite, glass, and acrylic plastic, *Tectonophysics,* **256,** 219–239.

Dobry, R. *et al*., 2000. New site coefficients and site classification system used in recent building seismic code provisions, *Earthq. Spectra,* **18,** 41–67.

Elkhoury, J.E., Brosky, E.E. & Agnew, D.C., 2006. Seismic waves increase permeability, *Nature,* **441,** 1135–1138.

Field, E.H., Johnson, P.A., Beresnev, I.A. & Zeng, Y., 1997. Non-linear ground-motion amplification by sediments during the 1994 Northridge earthquake, *Nature,* **390,** 599–602.

Gao, Y., Wang, P., Zheng, S., Wang, M. & Chen, Y.-T., 1998. Temporal changes in shear-wave splitting at an isolated swarm of small earthquakes in 1992 near Dongfang, Hainan Island, Southern China, *Geophys. J. Int.,* **135,** 102–112.

Gerst, A. & Savage, M.K., 2004. Seismic anisotropy beneath Ruapehu Volcano: a possible eruption forecasting tool, *Science,* **306,** 1543–1547.

Hall, S.A., Kendall, J.-M., Maddock, J. & Fisher, Q., 2008. Crack density tensor inversion for analysis of changes in rock frame architecture, *Geophys. J. Int.,* **173,** 577–592.

Hiramatsu, Y., Honma, H., Saiga, A., Furumoto, M. & Ooida, T., 2005. Seismological evidence on characteristic time of crack healing in the shallow crust, *Geophys. Res. Lett.,* **32,** L09304, doi:10.1029/2005GL022657.

Hung, J.-H., Wiltschko, D.V., Lin, H.-C., Hickman, J.B., Fang, P. & Bock, Y., 1999. Structure and motion of the southwestern Taiwan fold and thrust belt, *TAO,* **10**(3), 543–568.

Ikuta, R. & Yamaoka, K., 2004. Temporal variation in the shear wave anisotropy detected using the Accurately Controlled Routinely Operated Signal System (ACROSS), *J. geophys. Res.,* **109,** B09305, doi:10.1029/2003JB002901.

Jin, A. & Aki, K., 1986. Temporal change in coda Q before the Tangshan earthquake of 1976 and the Haicheng earthquake of 1975, *J. geophys. Res.,* **91,** 665–673.

Johnson, P.A. & Jia, X., 2005. Nonlinear dynamics, granular media and dynamic earthquake triggering, *Nature,* **437,** 871–874.

Johnson, P.A. & Sutin, A., 2005. Slow dynamics and anomalous fast dynamics in diverse solids, *J. acoust. Soc. Am.,* **117,** 124–130.

Jónsson, S., Segall, P., Pedersen, R. & Björnsson, G., 2003. Post-earthquake ground movements correlated to pore-pressure transients, *Nature,* **424,** 179–183.

Jurkevics, A., 1988. Polarization analysis of three-component array data, *Bull. seism. Soc. Am.,* **78,** 1725–1743.

Kanamori, H. & Fuis, G., 1976. Variation of *P*-wave velocity before and after the Galway Lake earthquake (ML = 5.2) and the Goat Mountain earthquakes (ML = 4.7, 4.7), 1975, in the Mojave desert, California, *Bull. seism. Soc. Am.,* **66,** 2027–2037.

Karabulut, H. & Bouchon, M., 2007. Spatial variability and non-linearity of strong ground motion near a fault, *Geophys. J. Int.,* **170,** 262–274, doi:10.1111/j.1365–246X.2007.03406.x.501.

Kern, H. & Wenk, H.R., 1990. Fabric-related velocity anisotropy and shear wave splitting in rocks from Santa Rosa Mylonite Zone, California, *J. geophys. Res.,* **95**(B7), 11 213–11 223.

Kuo, K.-W., 1994. The geological character of the CWB Strong Motion Network: Chianan area, Central Weather Bureau Report, CW83–1A-12, 98. (in Chinese).

Lee, C.-T., Cheng, C.-T., Liao, C.-W. & Tsai, Y.-B., 2001. Site classication of Taiwan free-field strong-motion stations, *Bull. seism. Soc. Am.,* **94**(5), 1283–1297.

Li, Y.-G., Vidale, J.E., Aki, K., Xu, F. & Burdette, T., 1998. Evidence of shallow fault zone strengthening after the 1992 M7.5 Landers, California, earthquake, *Science,* **279,** 217–219.

Li, Y.-G., Chen, P., Cochran, E.S., Vidale, J.E. & Burdette, T., 2006. Seismic evidence for rock damage and healing on the San Andreas Fault associated with the 2004 M 6.0 Parkfield earthquake, *Bull. seism. Soc. Am.,* **96**(4B), S349–S363.

Liu, Y., Teng, T.-L. & Ben-Zion, Y., 2004. Systematic analysis of shear-wave splitting in the aftershock zone of the 1999 Chi-Chi, Taiwan, Earthquake: Shallow crustal anisotropy and lack of precursory variations, *Bull. seism. Soc. Am.,* **94,** 2300–2347.

Liu, Y., Ben-Zion, Y. & Teng, T.-L., 2005a. Reply to "Comment on 'Systematic analysis of shear-wave splitting in the aftershock zone of the 1999 Chi-Chi, Taiwan, earthquake: shallow crustal anisotropy and lack of precursory changes,' by Yunfeng Liu, Ta-Liang Teng, and Yehuda Ben-Zion," by Stuart Crampin and Yuan Gao, *Bull. seism. Soc. Am.,* **95,** 361–366.

Liu, Y., Teng, T.-L. & Ben-Zion, Y., 2005b. Near-surface seismic anisotropy, attenuation and dispersion in the aftershock region of the 1999 Chi-Chi Earthquake, *Geophys. J. Int.,* **160,** 695–706.

Liu, Y., Zhang, H., Thurber, C. & Roecker, S., 2008. Shear wave anisotropy in the crust around the San Andreas fault near Parkfield: spatial and temporal analysis, *Geophys. J. Int.,* **172,** 957–970.

Lyakhovsky, V., Ben-Zion, Y. & Agnon, A., 1997. Distributed damage, faulting and friction, *J. geophys. Res.,* **102,** 27 635–27 649.

Lyakhovsky, V., Ben-zion, Y. & Agnon, A., 2005. A viscoelastic damage rheology and rate- and state-dependent friction, *Geophys. J. Int.,* **161,** 179–190, doi:10.1111/j.1365–246X.2005.02583.x.

Ma, S., 2008. A physical model for widespread near-surface and fault zone damage induced by earthquakes, *Geochem. Geophys. Geosyst.,* **9,** Q11009, doi:10.1029/2008GC002231.

Manga, M. & Brodsky, E., 2006. Seismic triggering of eruptions in the far field: volcanoes and geysers, *Annu. Rev. Earth planet. Sci.,* **34,** 263–291.

Manga, M. & Wang, C.-Y., 2007. Earthquake hydrology, in *Treatise on Geophysics,* Vol. 4, pp. 293–320, ed. Schubert, G., Elsevier Science, Amsterdam.

Marone, C., 1998. Laboratory-derived friction laws and their application to seismic faulting, *Annu. Rev. Earth planet. Sci.,* **26,** 643–696.

Matsumoto, S., Obara, K., Yoshimoto, K., Saito, T., Ito, A. & Hasegawa, A., 2001. Temporal change in *P*-wave scatterer distribution associated with the M6.1 earthquake near Iwate volcano, northeastern Japan, *Geophys. J. Int.,* **145,** 48–58.

Mavko, G., Mukerji, T. & Dvorkin, J., 1998. *The Rock Physics Handbook: Tools for Seismic Analysis of Porous Media,* Cambridge University Press, Cambridge, 340 pp.

McEvilly, T.V. & Johnson, L.R., 1974. Stability of *P* and *S* velocities from central California quarry blasts, *Bull. seism. Soc. Am.,* **64,** 343–353.

Menke, W. & Schaff, D., 2004. Absolute earthquake locations with differential data, *Bull. seism. Soc. Am.,* **94,** 2254–2264.

Miller, V. & Savage, M., 2001. Changes in seismic anisotropy after volcanic eruptions: evidence from Mount Ruapehu, *Science,* **293,** 2231–2233.

Munson, C.G., Thurber, C.H., Li, Y. & Okubo, P.G., 1995. Crustal shear wave anisotropy in southern Hawaii: spatial and temporal analysis, *J. geophys. Res.,* **100**(B10), 20 367–20 377.

Niu, F., Silver, P.G., Nadeau, R.M. & McEvilly, T.V., 2003. Stress-induced migration of seismic scatterers associated with the 1993 Parkfield aseismic transient event, *Nature,* **426,** 544–548.

Niu, F., Silver, P.G., Daley, T., Cheng, X. & Majer, E., 2008. Preseismic velocity changes observed from active source monitoring at the Parkfield SAFOD drill site, *Nature,* **454,** 204–208.

Nur, A., 1971. Effects of stress on velocity anisotropy in rocks with cracks, *J. geophys. Res.,* **76,** 2022–2034.

Nur, A. & Simmons, G., 1969. The effect of saturation on velocity in low porosity rocks, *Earth planet. Sci. Lett.,* **7,** 183–193.

Nuttli, O., 1961. The effect of the Earth's surface on the S wave particle motion, *Bull. seism. Soc. Am.,* **51**(2), 237–246.

Peng, Z. & Ben-Zion, Y., 2004. Systematic analysis of crustal anisotropy along the Karadere-Duzce branch of the North Anatolian fault, *Geophys. J. Int.,* **159,** 253–274.

Peng, Z. & Ben-Zion, Y., 2005. Spatio-temporal variations of crustal anisotropy from similar events in aftershocks of the 1999 M7.4 İzmit and M7.1 Duzce, Turkey, earthquake sequences, *Geophys. J. Int.,* **160,** 1027–1043.

Peng, Z. & Ben-Zion, Y., 2006. Temporal changes of shallow seismic velocity around the Karadere-Duzce branch of the north Anatolian fault and strong ground motion, *Pure appl. Geophys.,* **163,** 567–599, doi:10.1007/s00024–005-0034–6.

Peng, Z., Vidale, J.E., Marone, C. & Rubin, A., 2005. Systematic variations in recurrence interval and moment of repeating aftershocks, *Geophys. Res. Lett.,* **32**(15), L15301, doi:10.1029/2005GL022626.

Poupinet, G., Ellsworth, W.L. & Frechet, J., 1984. Monitoring velocity variations in the crust using earthquake doublets: An application to the Calaveras Fault, California, *J. geophys. Res.,* **89,** 5719–5731.

Press, W., Flannery, B., Teukolsky, S. & Vetterling, W., 1986. *Numerical Recipes,* Cambridge University Press, Cambridge.

Rojstaczer, S.A., Wolf, S.C. & Michel, R.L., 1995. Permeability enhancement in the shallow crust as a cause of earthquake-induced hydrological changes, *Nature,* **373,** 237–239.

Rubinstein, J.L. & Beroza, G.C., 2004a. Evidence for Widespread Nonlinear Strong Ground Motion in the M_w 6.9 Loma Prieta Earthquake, *Bull. seism. Soc. Am.,* **94,** 1595–1608.

Rubinstein, J.L. & Beroza, G.C., 2004b. Nonlinear strong ground motion in the ML5.4 Chittenden earthquake: evidence that pre-existing damage increases susceptibility to further damage, *Geophys. Res. Lett.,* **31,** L23614, doi:10.1029/2004GL021357.

Rubinstein, J.L. & Beroza, G.C., 2005. Depth constraints on nonlinear strong ground motion, *Geophys. Res. Lett.,* **32,** L14313, doi:10.1029/2005GL023189.

Rubinstein, J.L., Uchida, N. & Beroza, G.C., 2007. Seismic velocity reductions caused by the 2003 Tokachi-Oki earthquake, *J. geophys. Res.,* **112,** B05315, doi:10.1029/2006JB004440.

Saiga, A., Hiramatsu, Y., Ooida, T. & Yamaoka, K., 2003. Spatial variation in the crustal anisotropy and its temporal variation associated with a moderate-sized earthquake in the Tokai region, central Japan, *Geophys. J. Int.,* **154,** 695–705.

Savage, M.K., 1999. Seismic anisotropy and mantle deformation: what have we learned from shear wave splitting? *Rev. Geophys.,* **37**(1), 65–106.

Savage, M.K., Peppin, W.A. & Vetter, U.R., 1990. Shear wave anisotropy and stress direction in and near Long Valley Caldera, California, 1979–1988, *J. geophys. Res.,* **95**(B7), 11 165–11 177.

Sawazaki, K., Sato, H., Nakahara, H. & Nishimura, T., 2006. Temporal change in site response caused by earthquake strong motion as revealed from coda spectral ratio measurement, *Geophys. Res. Lett.,* **33,** L21303, doi:10.1029/2006GL027938.

Sawazaki, K., Sato, H., Nakahara, H. & Nishimura, T., 2009. Time-lapse changes of seismic velocity in the shallow ground caused by strong ground motion shock of the 2000 Western-Tottori Earthquake, Japan, as revealed from coda deconvolution analysis, *Bull. seism. Soc. Am.,* **99,** 352–366.

Schaff, D.P. & Beroza, G.C., 2004. Coseismic and postseismic velocity changes measured by repeating earthquakes, *J. geophys. Res.,* **109,** B10302, doi:10.1029/2004JB003011.

Scholz, C.H., 1968. The frequency-magnitude relation of microfracturing in rock and its relation to earthquakes, *Bull. seism. Soc. Am.,* **58,** 399–415.

Scholz, C.H., 2002. *The Mechanics of Earthquakes and Faulting,* 2nd edn, Cambridge University Press, New York, 471 pp.

Seher, T. & Main, I.G., 2004. A statistical evaluation of a 'stress-forecast' earthquake, *Geophys. J. Int.,* **157,** 187–193.

Shin, T.-C. & Teng, T.-L., 2001. An overview of the 1999 Chi-Chi, Taiwan, Earthquake, *Bull. seism. Soc. Am.,* **91**(5), 895–913.

Silver, P.G., Daley, T.M., Niu, F. & Majer, E.L., 2007. Active source monitoring of cross-well seismic travel time for stress-induced changes, *Bull. seism. Soc. Am.,* **97**(1B), 281–293, doi:10.1785/0120060120.

Tadokoro, K. & Ando, M., 2002. Evidence for rapid fault healing derived from temporal changes in S wave splitting, *Geophys. Res. Lett.,* **29**(4), 1047, doi:10.1029/2001GL013644.

Taira, T., Silver, P.G., Niu, F. & Nadeau, R.M., 2008. Detecting seismogenic stress evolution and constraining fault zone rheology in the San Andreas Fault following the 2004 Parkfield earthquake, *J. geophys. Res.,* **113,** B03303, doi:10.1029/2007JB005151.

Taira, T., Silver, P.G., Niu, F. & Nadeau, R.M., 2009. Seismic evidence for remote triggering of fault-strength changes on the San Andreas fault at Parkfield, *Nature,* **461,** 636–640.

Tai-Tech, Geotechnical & Construction Co., Ltd., 2000. The Hydrogeological Survey and Liquefaction Analysis Report, National Taiwan University, Taipei (in Chinese).

Teanby, N., Kendall, J.-M., Jones, R.H. & Barkved, O., 2004. Stress-induced temporal variations in seismic anisotropy observed in microseismic data, *Geophys. J. Int.,* **156,** 459–466.

TenCate, J.A., Smith, E. & Guyer, R.A., 2000. Universal slow dynamics in granular solids, *Phys. Rev. Lett.,* **85,** 1020–1023.

Toteva, T., Peng, Z. & Zhao, P., 2008. Temporal changes in near-surface layers and deep fault zone scatterers after the 2004 M_w6.0 Parkfield earthquake observed by the UPSAR, *EOS, Trans. Am. Geophys. Un.,* **89**(53), Fall Meet. Suppl., Abstract S53A-1816.

Valcke, S., Casey, M., Lloyd, G., Kendall, J.-M. & Fisher, Q., 2006. Lattice preferred orientation and seismic anisotropy in sedimentary rocks, *Geophys. J. Int.,* **166,** 652–666.

Vidale, J.E. & Li, Y.-G., 2003. Damage to the shallow Landers fault from the nearby Hector Mine earthquake, *Nature,* **421,** 524–526.

Wang, C.-Y. & Chia, Y., 2008. Wenchuan earthquake enhanced crustal permeability in Taiwan, *EOS, Trans. Am. Geophys. Un.,* **89**(53), Fall Meet. Suppl., Abstract U23B-0065.

Wang, C.-Y., Wang, C.-H. & Manga, M, 2004. Coseismic release of water from mountains: Evidence from the 1999 ($M_w = 7.5$) Chi-Chi, Taiwan, earthquake, *Geology,* **32**(9), 769–772. .

Wang, C., Chia, Y., Wang, P. & Dreger, D., 2009. Role of *S* waves and Love waves in coseismic permeability enhancement, *Geophys. Res. Lett.,* **36,** L09404, doi:10.1029/2009GL037330.

Wen, S., Chen, C.-H. & Teng, T.-L., 2008. Ruptures in a highly fractured upper crust, *Pure appl. Geophys.,* **165,** 201–213, doi:10.1007/s00024–008-0297–9.

Wessel, P. & Smith, W.H.F., 1998. New, improved version of the Generic Mapping Tools released, *EOS, Trans. Am. Geophys. Un.,* **79,** 579.

Whitcomb, J.H., Garmany, J.E. & Anderson, D.L., 1973. Earthquake prediction: variation of seismic velocities before the San Francisco earthquake, *Science,* **180,** 632–635.

Wilks, D.S., 2006. *Statistical Methods in the Atmospheric Sciences,* 2nd edn, Vol. 91, pp. 138–140, Academic Press, USA.

Wu, Y.-M. & Teng, T.-L., 2002. A virtual subnetwork approach to earthquake early warning, *Bull. seism. Soc. Am.,* **92,** 2008–2018.

Wu, Y.-M., Chang, C.-H., Hsiao, N.-C. & Wu, F.T., 2003. Relocation of the 1998 Rueyli, Taiwan, earthquake sequence using three-dimensions velocity structure with stations corrections, *Terres., Atmos. Ocean. Sci.,* **14,** 421–430.

Wu, C., Peng, Z. & Ben-Zion, Y., 2009a. Non-linearity and temporal changes of fault zone site response associated with strong ground motion, *Geophys. J. Int.,* **176,** 265–278, doi:10.1111/j.1365–246X.2008.04005.x.

Wu, C., Peng, Z. & Assimaki, D., 2009b. Temporal changes in site response associated with strong ground motion of 2004 $M_w6.6$ Mid-Niigata earthquake sequences in Japan, *Bull. seism. Soc. Am.,* doi:10.1785/0120090108.

Yu, S.-B. *et al.*, 2001. Preseismic deformation and coseismic displacements associated with the 1999 Chi-Chi, Taiwan, earthquake, *Bull. seism. Soc. Am.,* **91,** 995–1012.

Zhao, P. & Peng, Z., 2009. Depth extent of damage zones around the central Calaveras fault from waveform analysis of repeating earthquakes, *Geophys. J. Int.,* doi:10.1111/j.1365-246X.2009.04385.x (this issue).

Zinke, J.C. & Zoback, M.D., 2000. Structure-related and stress-induced shear-wave velocity anisotropy: observations from microearthquakes near the Calaveras Fault in Central California, *Bull. seism. Soc. Am.,* **90,** 1305–1312.

APPENDIX A

We calculate the true incident angle of each event from the particle motion of first arrival *P* wave. In detail, we first cut 0.2-s time window to include the direct upgoing *P*-wave, and then rotate two horizontal components to the directions that are parallel and perpendicular to the back azimuth. Next, we use the principal component analysis (PCA) of Jurkevics (1988) to measure the angle between the first PCA axis and the vertical direction, which is defined as the true incident angle. We have tested this method by using three-component synthesis seismogram, and the observed incident angle matches the one used to generate the original synthesis seismograms well. Fig. A1 show a comparison of the true incident angle and the apparent incident angle (simply computed from the ratio between the epicentral distance and depth). We find that most (90 per cent) of the true incident angles were smaller than 20°, and the true incident angles are smaller than the apparent incident angles. These
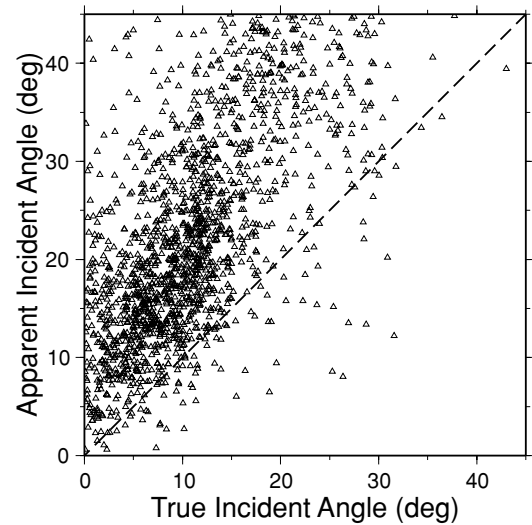
Figure A1. A comparison between true incident angle and apparent incident angle. The diagonal dotted line marks the one to one ratio between these two values.

observations are consistent with the inference that the seismic rays tend to bend towards vertical with decreasing seismic velocities and densities in the shallow crust.

APPENDIX B

Assuming a homogeneous half space and plane wave incidence, we derive the relationship between the incident angle *i* the TD of upgoing and surface reflected waves. The schematic diagram is shown in Fig. B1(a). For a vertical incidence with $i = 0°$, the TD is given by

$$TD = \Delta s / v = 2d/v, \tag{B1}$$

where *d* is the depth of the borehole seismometer, *v* is the seismic wave velocity, and Δs is the total propagation distance between the upgoing and surface reflected waves.

For a plane wave with incident angle of *i*, the total propagation distance between the upgoing and surface reflected waves can be expressed as

$$\Delta s = DE + EA. \tag{B2}$$

The line segment *EA* can be expressed in terms of the depth *d* and the incident angle *i* as

$$L = EA = EC = d/\cos(i). \tag{B3}$$

The line segment *AC* can be written as
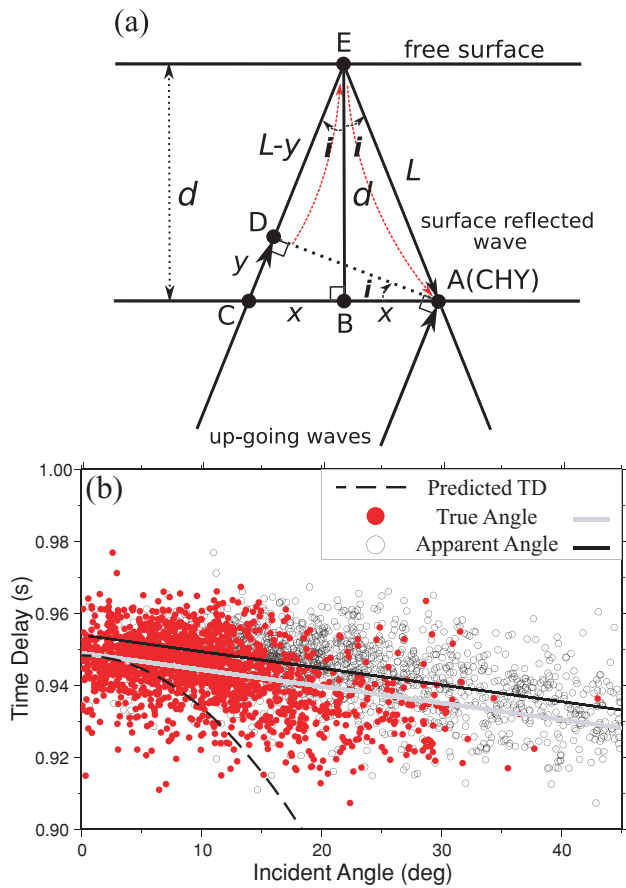
$$AC = 2 \cdot AB = 2 \cdot d\tan(i). \tag{B4}$$

The line segment *CD* can be expressed in terms of the line segment *AC* and the incident angle *i* as

$$CD = AC \cdot \sin(i) = 2 \cdot d\tan(i) \cdot \sin(i). \tag{B5}$$

Hence, the total distance Δs is

$$\Delta s = DE + EA = 2L - CD$$
$$= 2d/\cos(i) - 2d \cdot [\sin(i)/\cos(i)] \cdot \sin(i)$$
$$= 2d\cos(i). \tag{B6}$$

Figure B1. (a) Schematic diagram illustrating the geometry of the upgoing and surface-reflected waves recorded by a borehole seismometer (at the depth of d) for non-vertical incident waves with an incident angle of i. The red-dotted curve represents the expected true incident ray path. (b) A comparison among the predicted TDs, observed TDs versus true (red circle) and apparent (white circle) incident angles. The predicted TD is calculated from the total separation distances between the upgoing and surface reflected waves using eq. (B8). The observed TDs are measured in the E (fast) component and is the same as shown in Fig. 4(c).

So the TD between the upgoing and surface reflected waves is

$$TD = \Delta s/v = 2d\cos(i)/v. \tag{B7}$$

For a vertical incidence with $i = 0°$, eq. B7 returns to eq. B1. If we use the depth of the CHY station $d = 200$ m, and the fast S wave velocity $v = 421.8$ m s^{-1} before the Chia-Yi main shock, we obtain

$$TD = 2d\cos(i)/v = 2 \cdot 200 \cdot \cos(i)/421.8 = 0.9483\cos(i). \tag{B8}$$

Fig. B1(b) shows the comparison between the predicted TDs (i.e. the dotted curving line calculated from eq. B8) with increasing incident angle i, and observed TDs versus the true incident angles (i.e. the same as in Fig. 4c) and apparent incident angles on the E component. The procedure for calculating the true incident angle is given in Appendix A, and the apparent angles are computed directly using the ratio of the epicentral distance and depth. The predicted TD values fall more rapidly when the incident angle is larger than 10° due to the shorter straight ray path. However, in reality the waves will follow the curving ray path (i.e. red dotted line in Fig. B1a) due to increasing velocity with increasing depth, resulted in a longer TD than that predicted by the straight-line ray path.

SUPPORTING INFORMATION

Additional Supporting Information may be found in the online version of this article:

Table S1. Time delays and other related parameters measured at different components for different groups of earthquakes used in this study.

Please note: Wiley-Blackwell are not responsible for the content or functionality of any supporting materials supplied by the authors. Any queries (other than missing material) should be directed to the corresponding author for the article.